Icarus **145**, 428–444 (2000)
doi:10.1006/icar.2000.6342, available online at http://www.idealibrary.com on IDEAL®

Seasonal Photochemical and Meridional Transport Model for the Stratosphere of Titan

James R. Dire

Department of Science, U. S. Coast Guard Academy, 27 Mohegan Avenue, New London, Connecticut 06320
E-mail: dire@dcseq.uscga.edu

Received March 19, 1999; revised December 13, 1999

A two-dimensional photochemical transport model is developed for Titan's stratosphere. Transformed Eulerian mean equations are used to determine the meridional circulation. Mechanical forcing is modeled using eddy and Rayleigh friction, while thermal forcing is provided by Newtonian and eddy heating. The model contains 117 photolysis, chemical, and condensation reactions for 22 hydrocarbon species along with atomic and molecular hydrogen. The method of conservation of second-order moments is used for the meridional and vertical advection calculations (Prather, M. J. 1986. *J. Geophys. Res.* 91, 6671–6681.).

Coustenis and Bézard (1995. *Icarus* 115, 126–140) analyzed the Voyager IRIS data to calculate hydrocarbon abundances from 53°S to 70°N. They determined that the ethane mixing ratio was approximately constant for all sampled latitudes. In the absence of meridional transport, photochemistry would yield higher concentrations of C_2 and C_3 hydrocarbon species near the equator than near the poles. Meridional advection results in enough tracer transport from low to high latitudes that the latitudinal distributions for ethane are much more uniform.

The model shows methane is well mixed in Titan's stratosphere. Model mixing ratios for ethane and propane agree well with Voyager IRIS data; however, the model overestimates the abundances of acetylene and diacetylene. The model abundance for methylacetylene is within the Voyager observational uncertainty, but the abundance for mid-southern latitudes is at the high end of this uncertainty. The model does not accurately reproduce the observed ethylene abundances.

Mid-latitude column densities (above 5 mbar) for ethane, propane, acetylene, and methylacetylene vary seasonal by 10, 14, 9.5, and 12%, respectively. Large seasonal variations for short-lived chemical species results in significant seasonal variations in the chemical production rates for organic polymers at middle and high latitudes.

Key Words: **Titan; atmosphere, composition; photochemistry.**

1. INTRODUCTION

The Voyager 1 spacecraft encountered Titan November 13, 1980, passing within 3500 km of the surface. The ultraviolet instrument detected the presence of nitrogen, leading to the conclusion that the atmosphere is predominantly molecular nitrogen (Broadfoot *et al.* 1981, Strobel and Shemansky 1982). The infrared instrument (IRIS) found strong emission features from CH_4, C_2H_2, C_2H_4, C_2H_6, and HCN (Hanel *et al.* 1981). Also identified in Titan's atmosphere were C_3H_8, CH_3CCH, C_4H_2, HC_3N, C_2N_2, and CO_2 (Kunde *et al.* 1981, Maguire *et al.* 1981, and Samuelson *et al.* 1983).

Visual imaging of Titan (Smith *et al.* 1981) did not reveal the surface but instead a global haze layer surrounding the satellite. Titan's northern hemisphere was found to be much darker and redder than the southern hemisphere. Southern mid-latitudes had albedos 25% greater than northern mid-latitudes. Also, in the northern hemisphere there was a dark polar hood above latitude 60°. The albedo of this dark polar region was approximately 7% less than northern mid-latitudes. No such feature was seen at the south pole. It was noted during the Voyager 1 encounter, which occurred near the northern hemisphere vernal equinox, that the albedo boundary between the hemispheres was at latitude 5°S, having moved south by 10° since the flyby of Pioneer 11 fourteen months earlier. This was opposite to the motion of the subsolar point and most likely an effect from Titan's 29.7 year seasonal cycle (Sromovsky *et al.* 1981). The hemispheric albedo asymmetry was reversed two seasons later as observed by the Hubble space telescope (Caldwell *et al.* 1992), confirming this seasonal effect.

A more complete analysis of the Voyager infrared data showed that latitudinal variations in brightness temperature existed in addition to the visual albedo variations. Spectra were taken for 200, 530, and 1304 cm^{-1} over a 6-h period when the spacecraft was within 200,000 km of Titan. The field of view was a third of Titan's radius. The brightness temperature at 200 cm^{-1} corresponds to roughly the tropopause temperature, with most of the opacity assumed to be due to CH_4 clouds just below the tropopause (Flasar *et al.* 1981). The northern hemisphere was found to be approximately 1 K warmer than the southern hemisphere at this wavenumber. The 530-cm^{-1} spectra probe very close to the surface and the brightness temperature should be near the actual surface temperature. At 530 cm^{-1} the spectra at low latitudes showed the northern hemisphere to be slightly warmer than the southern hemisphere, again by approximately 1 K, consistent with the tropopause temperature difference interpreted from the 200-cm^{-1} spectra.

0019-1035/00

The situation is much different in the upper stratosphere, where the radiative response time is estimated to be on the order of 1 year (Flasar *et al.* 1981). This is much longer than the 16-day rotational period of Titan, implying that diurnal temperature variations should be minimal, but it is much shorter than the seasonal period, implying that meridional upper stratospheric temperatures should not lag significantly behind the seasonal forcing. Since the Voyager flyby occurred near the northern spring equinox, hemispherically symmetric brightness temperatures should have been seen. However, the brightness temperatures in the upper stratosphere (0.3 mbar level) were not symmetric between the two hemispheres (Flasar *et al.* 1981). A more recent work by Coustenis and Bézard (1995) estimates the temperature difference from the IRIS data between 50°N and 53°S latitude to be 7 K at 1 mbar pressure, the south being warmer.

As previously mentioned, the asymmetry in the hemispheric temperatures was accompanied by asymmetries in the visible albedo of the satellite. The southern hemisphere had a higher temperature and was visually brighter. It is not known whether these two phenomena originated at different levels in the atmosphere. The hemispheric differences in brightness may be caused by (1) differences in height or number density of atmospheric species, (2) variations in particle size or composition, or (3) dynamics coupled with one of the above (Smith *et al.* 1981). Hutzell *et al.* (1996) developed a 2-D model to study the effect of atmospheric motion of Titan's haze layer. They were unable to produce the latitudinal distribution of reflectivity seen during the Voyager 1 encounter. Flasar and Conrath (1990) have made a case for a dynamical explanation of the observed infrared emissions, However, they have not ruled out the possibility of an asymmetry in the meridional distribution of opacity. They suggest that it may be necessary to supplement their model and explain all of the Voyager observations. Bézard *et al.* (1995) calculated that latitudinal variations in gas and haze composition alone could account for the temperature asymmetry without the need to invoke dynamical inertia. Photochemical and transport modeling is needed to explain any of these seasonal variations in opacity.

Prior to the Voyager I encounter with Saturn, theoretical studies of Titan's atmosphere only involved hydrocarbon photochemistry (Strobel 1974, Caldwell 1978, Allen *et al.* 1980). A comprehensive post-Voyager one-dimensional (1-D) photochemical model was developed for the atmosphere of Titan by Yung *et al.* (1984). Yung *et al.* (1984) investigated the photochemistry of simple molecules containing carbon, hydrogen, nitrogen, and oxygen in the atmosphere of Titan. They incorporated the most up-to-date chemical schemes and reaction rate coefficients at that time. For rate coefficients that were unknown, they made estimates based on similar reactions. They started with an atmosphere that contained N_2, CH_4, and H_2O. The amount of N_2 was held constant, CH_4 was given a fixed mixing ratio (0.02) at the lower boundary, and a constant downward flux of H_2O was assumed at the upper boundary. They incorporated 24 photolysis reactions, 65 chemical reactions involving hydrocarbons only, and 35 chemical reactions involving nitrogen- and oxygen-containing species.

Yung *et al.* (1984) performed their calculations using a latitude of 30°, assuming this was representataive of a global average, and incorporated eddy and molecular diffusion in the vertical direction. Their model set the lower boundary at the tropopause and the upper boundary at an altitude of 1160 km (except for H and H_2, where they used 1425 km for Jeans escape calculations). Their temperature profile was after Lindal *et al.* (1983) for the stratosphere, with an isothermal temperature profile for altitudes above the stratosphere. Setting diffusion boundary conditions for long-lived species at the tropopause and photochemical equilibrium for short-lived species, and only allowing H and H_2 to gravitationally escape, Yung *et al.* (1984) solved the continuity equation in spherical coordinates using a finite-difference iterative algorithm. They then compared their results to observational data from the Voyager studies.

The photochemical model of Yung *et al.* (1984) yielded a mixing ratio for CH_4 at the upper boundary, in excellent agreement with the results of the Voyager UVS experiment. Their values for the abundances of C_2H_6, H_2, HC_3N, and C_2N_2 were also consistent with the inferred Voyager analysis. For C_2H_4 the model was about a factor of 10 too low, while for C_2H_2 the model was a factor of 2 higher than Voyager IRIS observations. For C_4H_2 their model calculated abundance was 10–100 times lower than the observational estimates, while the CO calculated abundance was a factor of 3 higher than observed abundance.

More recent 1-D photochemical models were developed by Toublanc *et al.* (1995) and Lara *et al.* (1996). Both of these works had improvements over that by Yung *et al.* (1984) in that they used an updated CH_4 photodissociation scheme, an eddy diffusion coefficient profile constrained by more recent observational data, current values for chemical reaction rate coefficients, and a more rigorous treatment of the transfer of solar radiation. In addition, whereas Yung *et al.* assumed a CH_4 mixing ratio of 0.02 in the stratosphere, Toublanc *et al.* adopted a value of 0.016 and Lara *et al.* used a nominal value of 0.017.

Both of these recent models yielded a mole fraction for CH_4 at 1140 km of 10% compared to 8.3% from Yung *et al.* (1984) and $8 \pm 3\%$ from the Voyager UVS observations. Their results for C_2H_2 and C_2H_6 are much closer than Yung *et al.* to the inferred Voyager IRIS data for the lower stratosphere, but these two new models disagree by an order of magnitude on the ethane abundance in the upper stratosphere. Like Yung *et al.*, Toublanc *et al.* had difficulty matching the observed abundance for C_4H_2. Lara *et al.* had difficulty matching the observed abundances for both C_4H_2 and C_3H_8.

Although 1-D photochemical models are very useful for understanding the processes that are occurring in Titan's atmosphere, a two-dimensional (2-D) model is needed to increase our understanding of the observed seasonal variations. The purpose of this investigation is to develop a simple 2-D, zonally

averaged, photochemical transport model for the atmosphere of Titan and to use it to analyze latitudinal variations in hydrocarbon abundance in the stratosphere of Titan as the seasons progress.

2. TWO-DIMENSIONAL PHOTOCHEMICAL TRANSPORT MODELS

Two-dimensional photochemical transport models are inherently more complex than 1-D models. One-dimensional models typically incorporate local chemistry, photolysis, radiative transfer, and vertical eddy and molecular diffusion. These models use a specific latitude and season and assume diurnal and zonal averages. Two-dimensional photochemical transport models must also incorporate local chemistry, photolysis, radiative transfer, and eddy and molecular diffusion. In addition to these effects, a 2-D model must incorporate vertical and meridional transport of atmospheric species, as well as latitudinal variations in thermodynamic parameters, including seasonal insolation. Zonal averaging is usually assumed along surfaces that are constant with respect to the vertical coordinate.

To model tracer transport in a time-dependent 2-D photochemical model, the dynamical motion of the atmosphere must be calculated. This is usually done using a 2-D or 3-D general circulation model (GCM) that incorporates detailed solar heating and radiative cooling calculations. Many of these models, originally developed for the Earth's atmosphere, have been modified for studies of other planetary atmospheres. These GCM models, like the comprehensive 1-D photochemical models, are typically very computationally intensive by themselves. To date, no 2-D photochemical transport models have been developed for Titan. However, as this work will show, if appropriate approximations are made to reduce the computational complexity, a simple 2-D model can be used for a first-order study of the seasonal variation in hydrocarbon abundance in Titan's stratosphere.

All photochemical transport models must make use of the continuity equation as it applies to each atmospheric constituent. The continuity equation for the mixing ratio, μ_i, of the ith trace species is

$$\frac{\partial \mu_i}{\partial t} + \mathbf{v} \cdot \nabla \mu_i + \frac{1}{N} \nabla \cdot \phi_i = \frac{P_i}{N} - L_i \mu_i, \tag{1}$$

where

- t is time
- $\mathbf{v}$ is velocity
- P_i is photochemical production rate of the ith species per unit volume
- L_i is photochemical loss rate of the ith species
- N is number density of the background atmosphere
- ϕ_i is diffusive flux of the ith species.

The continuity equations for the trace species are coupled with dynamical and thermodynamical equations for which no analytical solutions exist. As in 1-D models, 2-D models must make use of numerical methods to solve for the distribution of each atmospheric constituent.

A comprehensive 2-D photochemical model was developed for the stratosphere of Uranus by McMillan (1992). In this model, a numerical technique known as operator-splitting was employed to solve the coupled equations. Using operator-splitting, Eq. (1) is rewritten as

$$\frac{\partial \mu_i}{\partial t} = \left[\frac{\partial \mu_i}{\partial t}\right]_{\text{photochemistry}} + \left[\frac{\partial \mu_i}{\partial t}\right]_{\text{advection}} + \left[\frac{\partial \mu_i}{\partial t}\right]_{\text{diffusion}}, \tag{2}$$

where

$$\left[\frac{\partial \mu_i}{\partial t}\right]_{\text{photochemistry}} = \frac{P_i}{N} - L_i \mu_i. \tag{3}$$

$$\left[\frac{\partial \mu_i}{\partial t}\right]_{\text{advection}} = -\mathbf{v} \cdot \nabla \mu_i, \tag{4}$$

and

$$\left[\frac{\partial \mu_i}{\partial t}\right]_{\text{diffusion}} = -\frac{1}{N} \nabla \cdot \phi_i. \tag{5}$$

The photochemical-transport model presented in this paper uses the techniques of operator-splitting. First, the atmosphere is divided into a numerical grid. Photochemical reaction calculations are performed to determine the chemical production and loss rates for each grid cell for the current time step. Equation (3) is then solved. Next, a dynamical model is used to determine the meridional circulation. The resulting velocity field is used to calculate the advective mass transport and Eq. (4) is solved. Finally, eddy and molecular diffusion are accounted for by solving Eq. (5). The process is repeated for the next time step. The next three sections will discuss the numerical techniques used to solve Eqs. (3)–(5).

3. HYDROCARBON PHOTOCHEMISTRY

The treatment of photochemistry in a 2-D photochemical transport model is very similar to its treatment in a 1-D model. This is because chemical reactions are essentially local processes that depend on the physical conditions and molecular concentrations of each species in each grid cell. However, the number of photons available to interact with a species that can be photodissociated does depend on the total number of absorbing species along the optical path to each grid cell. So, indirectly, the production and/or loss of some chemical species is dependent on non-local conditions.

In 1-D photochemical models, the optical path is chosen to be either vertically downward or vertically downward with the

incorporation of a factor to account for a diurnally averaged solar zenith angle. A 2-D time-dependent model must account for the variation of zenith angle with the latitude and season, but the basic physics is the same as in 1-D models. Photodissociation processes are treated similarly to those in Summers and Strobel (1989). The rate of photodissociation of a species, i, is given by

$$J_i(z) = \int_{\lambda_1}^{\lambda_2} \sigma_{i,\lambda} \Phi(z, \lambda)\, d\lambda. \quad (6)$$

Here, λ is the wavelength, $\sigma_{i,\lambda}$ is the absorption cross section as a function of wavelength, and $\Phi(z, \lambda)$ is the solar flux at altitude z and wavelength λ. The flux $\Phi(z, \lambda)$ has dimensions of photons per unit area per second per wavelength. The wavelength region for photodissociation is 1000–2600 Å. We can express $\Phi(z, \lambda)$ as a function of the diurnally averaged unattenuated flux at the top of the atmosphere, $\Phi_\infty(\lambda)$,

$$\Phi(z, \lambda) = \Phi_\infty(\lambda) \exp\left\{ -\int_z^\infty \left[\sum_i \sigma_{i,\lambda} n_i(z') \right] \alpha_{z'}\, dz' \right\}. \quad (7)$$

In Eq. (7), n_i is the number density of the ith photoreactive species and α is the Chapman function of the solar zenith angle (Lara *et al.* 1996).

In numerical form the integral in Eq. (6) is replaced with a summation over wavelength bins 50 Å wide. The flux due to Ly-α is treated separately and added to the summation. Equation (6) becomes

$$J_i(z) = \sigma_{i,Ly\text{-}\alpha} F(z, \lambda_{Ly\text{-}\alpha}) + \sum_{w=1}^{32} \sigma_{i,\lambda_w} F(z, \lambda_w), \quad (8)$$

where $F(z, \lambda)$ is the solar flux at altitude z and wavelength λ in dimensions of photons per unit area per second. In Eq. (8), the integration is replaced with a summation over all the vertical grid cells. This yields

$$F(z, \lambda) = F_\infty(\lambda) \exp\left\{ -\sum_k \left[\sum_i \sigma_{i,\lambda} n_i(k) \right] \alpha \Delta z \right\}. \quad (9)$$

Not explicitly shown in Eqs. (8) and (9) are the dependencies of the photolysis rate on the latitude and season. The photolysis rate $J_i(z)$ is really $J_i(\phi, z, t)$, where ϕ is the latitude and t is time. Corrections to Eqs. (8) and (9) to account for the latitude and seasonal dependence are found in Cogley and Borucki (1976). This work has adopts Cogley and Borucki's approximation 4 to perform these calculations. The unattenuated solar flux at the top of the atmosphere and the attenuation of the solar flux due to Titan's aerosols are treated in the same manner as in Lara *et al.* (1996).

The 24 chemical species considered in this model are listed in Table I. This list contains all C_1–C_3 hydrocarbons, several C_4 hydrocarbons important in the formation of polymers, and molecular and atomic hydrogen. Table II lists the photolysis reactions while Tables III and IV contain the termolecular and bimolecular chemical reactions, respectively. Condensation processes are treated identically to those in Yung *et al.* (1984).

TABLE I
Chemical Species Used in the Photochemical Model

Index	Formula	Name	Alternate name(s)
1	CH_4	methane	
2	C_2H_6	ethane	
3	C_2H_2	acetylene	ethyne
4	C_3H_8	propane	
5	CH_3CCH	methylacetylene	propyne, allylene
6	C_2H_4	ethylene	ethene
7	C_4H_2	diacetylene	1,3-butadiyne
8	C_3H_6	propylene	propene
9	CH_2CCH_2	allene	propadiene
10	C_3H_3	allenyl	propynyl
11	CH_3	methyl	
12	$^1CH_2$	methylene (excited state)	
13	$^3CH_2$	methylene (ground state)	
14	CH	methylidyne	
15	C_2H	ethynyl	
16	C_2H_3	vinyl	ethenyl
17	C_2H_5	ethyl	
18	C_3H_2	allenylcarbene	propynylidene
19	C_3H_5	allyl	propenyl, propylidene
20	C_3H_7	propyl	
21	C_4H	butadiynyl	
22	C_4H_3	butenynyl	butatrienyl
23	H	atomic hydrogen	
24	H_2	molecular hydrogen	

To solve for the abundance variations in each grid cell due to photochemistry, the time-dependent explicit finite difference form of Eq. (3) is employed:

$$\mu_i^n = \frac{P_i^{n-1} \Delta t}{N} + \left(1 - L_i^{n-1} \Delta t\right) \mu_i^{n-1}. \quad (10)$$

Solutions using Eq. (10) are accurate and stable for chemical species whose photochemical lifetimes are greater than the time step, Δt. For short-lived species, photochemical equilibrium is used to solve for the mixing ratios,

$$\mu_i^n = \frac{P_i^{n-1}}{L_i^{n-1} N}. \quad (11)$$

For the species that do not clearly fall into either the long-lived or the short-lived group, Eq. (10) is used to solve for their mixing ratios for grid cells in which their photochemical lifetimes exceed Δt. Equation (11) is used to solve for their mixing ratios for grid cells in which their photochemical lifetimes are less than Δt.

4. DYNAMICAL MODEL FOR TITAN'S STRATOSPHERE

For Titan, the Coriolis parameter is sufficiently small, due to its slow rotational rate, that cyclostrophic terms cannot be

TABLE II
Photodissociation Reactions for Titan Model Atmosphere

Index	Reactions	Quantum yield		Reference
		Ly-α	Other	
P11	$CH_4 + h\nu \rightarrow {}^1CH_2 + H_2$	0.22	0	Heck *et al.* 1996
P12	$CH_4 + h\nu \rightarrow CH_3 + H$	0.67	1	Heck *et al.* 1996
P13	$CH_4 + h\nu \rightarrow CH + H + H_2$	0.11	0	Heck *et al.* 1996
P21	$C_2H_6 + h\nu \rightarrow C_2H_4 + H_2$	0.12	0.56	Akimoto *et al.* 1965
P22	$C_2H_6 + h\nu \rightarrow C_2H_4 + 2H$	0.3	0.14	Hampson *et al.* 1965
P23	$C_2H_6 + h\nu \rightarrow C_2H_2 + 2H_2$	0.25	0.27	Lias *et al.* 1970
P24	$C_2H_6 + h\nu \rightarrow CH_4 + {}^1CH_2$	0.25	0.02	Mount *et al.* 1978
P25	$C_2H_6 + h\nu \rightarrow 2CH_3$	0.08	0.01	Mount *et al.* 1978
P31	$C_2H_2 + h\nu \rightarrow C_2H + H$	0.3	0.06	Nakayawa *et al.* 1964
P32	$C_2H_2 + h\nu \rightarrow C_2 + H_2$	0.1	0.1	Okabe 1981, 1983
P41	$C_3H_8 + h\nu \rightarrow C_3H_6 + H_2$	0.33	0.94	Calvert and Pitts 1966
P42	$C_3H_8 + h\nu \rightarrow C_2H_6 + {}^1CH_2$	0.09	0	Calvert and Pitts 1966
P43	$C_3H_8 + h\nu \rightarrow C_2H_5 + CH_3$	0.38	0	Calvert and Pitts 1966
P44	$C_3H_8 + h\nu \rightarrow C_2H_4 + CH_4$	0.2	0.06	Calvert and Pitts 1966
P51	$CH_3CCH + h\nu \rightarrow C_3H_3 + H$	0.4	0.4	Stief *et al.* 1971
P52	$CH_3CCH + h\nu \rightarrow C_3H_2 + H_2$	0.15	0.15	Hamai *et al.* 1979
P53	$CH_3CCH + h\nu \rightarrow CH_3 + C_2H$	0.2	0.2	Hamai *et al.* 1979
P61	$C_2H_4 + h\nu \rightarrow C_2H_2 + H_2$	0.51	0.51	Zelikoff *et al.* 1953
P62	$C_2H_4 + h\nu \rightarrow C_2H_2 + 2H$	0.49	0.49	Back *et al.* 1967
P71	$C_4H_2 + h\nu \rightarrow C_4H + H$	0.2	0.03	Summers *et al.* 1989
P72	$C_4H_2 + h\nu \rightarrow 2C_2H$	0.03	0.01	Summers *et al.* 1989
P73	$C_4H_2 + h\nu \rightarrow C_2H_2 + C_2$	0.1	0.02	Summers *et al.* 1989
P74	$C_4H_2 + h\nu \rightarrow C_4H_2{}^{**}$	0.67	0.67	Summers *et al.* 1989
P81	$C_3H_6 + h\nu \rightarrow CH_2CCH_2 + H_2$	0.57	0.57	Calvert and Pitts 1966
P82	$C_3H_6 + h\nu \rightarrow C_2H_4 + CH_2$	0.02	0.02	Borrell *et al.* 1971
P83	$C_3H_6 + h\nu \rightarrow C_2H_2 + CH_3 + H$	0.34	0.34	Collin *et al.* 1979
P84	$C_3H_6 + h\nu \rightarrow C_2H + CH_4 + H$	0.05	0.05	Collin 1973
P91	$CH_2CCH_2 + h\nu \rightarrow C_3H_3 + H$	0.4	0.4	Sutcliffe *et al.* 1952
P92	$CH_2CCH_2 + h\nu \rightarrow C_3H_2 + H_2$	0.15	0.15	Rabelais *et al.* 1971
P93	$CH_2CCH_2 + h\nu \rightarrow C_2H_2 + CH_2$	0.06	0.06	Heller and Milne 1978
P10	$C_3H_3 + h\nu \rightarrow C_3H_2 + H$	1	1	Jacox *et al.* 1974

neglected in dynamical equations. The transformed Eulerian-mean (TEM) equations (Andrews *et al.* 1987) are used for the meridional circulation in Titan's stratosphere since they are easily solved in the cyclostrophic regime. The meridional and vertical velocities used in the TEM equations are good approximations for advective transport calculations (Andrews *et al.* 1987).

In spherical log pressure coordinates the TEM primitive set of equations is

$$\frac{\partial \bar{u}}{\partial t} + \bar{v}^* \left[\frac{1}{a \cos\phi} \frac{\partial (\bar{u} \cos\phi)}{\partial \phi} - f \right] + \bar{w}^* \frac{\partial \bar{u}}{\partial z} - \bar{X} = \frac{1}{\rho_0 r \cos\phi} \nabla \cdot \mathbf{F} \tag{12}$$

$$\bar{u} \left[f + \frac{\bar{u} \tan\phi}{a} \right] + \frac{1}{a} \frac{\partial \bar{\Phi}}{\partial \phi} = G \tag{13}$$

$$\frac{\partial \bar{\Phi}}{\partial z} - \frac{R}{H_0} \bar{\theta} \exp\left(-\frac{\kappa z}{H_0} \right) = 0 \tag{14}$$

$$\frac{1}{a \cos\phi} \frac{\partial}{\partial \phi} (\bar{v}^* \cos\phi) + \frac{1}{\rho_0} \frac{\partial}{\partial z} (\rho_0 \bar{w}^*) = 0 \tag{15}$$

$$\frac{\partial \bar{\theta}}{\partial t} + \frac{\bar{v}^*}{a} \frac{\partial \bar{\theta}}{\partial \phi} + \bar{w}^* \frac{\partial \bar{\theta}}{\partial z} - \bar{Q} = -\frac{1}{\rho_0} \left[\frac{1}{a} \frac{\partial}{\partial z} \left(\rho_0 \frac{\overline{v'\theta'}}{(\partial \bar{\theta}/\partial z)} \frac{\partial \bar{\theta}}{\partial \phi} \right) + \frac{\partial}{\partial z} (\rho_0 \overline{w'\theta'}) \right]. \tag{16}$$

Equations (12) and (13) are the zonal and meridional momentum balances, respectively. Equation (14) is called the hydrostatic equation, Eq. (15) is the continuity equation, and Eq. (16) is the heat equation. The symbols for these equations are defined in Table V. The bars denote zonal averages, the primes denote deviations from the zonal averages, and the asterisks denote residual velocities (Andrews *et al.* 1987).

TABLE III
Termolecular Chemical Reactions

	Reaction	Rate coefficients[a]	Reference
1	$H + H + M \rightarrow H_2 + M$	$k_0 = 2.5 \times 10^{-31}\ T^{-0.6}$ $k_\infty = 1.0 \times 10^{-11}$	Baulch *et al.* 1992
2	$CH + H_2 + M \rightarrow CH_3 + M$	$k_0 = 3.8 \times 10^{-29}\ e^{-20/T}$ $k_\infty = 2.4 \times 10^{-12}\ e^{523/T}$	Gladstone *et al.* 1996
3	$^3CH_2 + H + M \rightarrow CH_3 + M$	$k_0 = 3.1 \times 10^{-30}\ e^{-457/T}$ $k_\infty = 1.5 \times 10^{-11}$	Summers and Strobel 1989
4	$C_3H_7 + H + M \rightarrow C_3H_8 + M$	$k_0 = 1.0 \times 10^{-22}\ e^{341/T}$ $k_\infty = 1.7 \times 10^{-10}$	Gladstone *et al.* 1996
5	$C_2H_3 + C_2H_3 + M \rightarrow C_4H_6 + M$	$k_0 = 8.76 \times 10^{-6}\ e^{-1390/T}\ T^{-7.0}$ $k_\infty = 8.2 \times 10^{-11}$	Gladstone *et al.* 1996
6	$CH_3 + H + M \rightarrow CH_4 + M$	$k_0 = 3.8 \times 10^{-28}\ e^{-20/T}$ $k_\infty = 2.1 \times 10^{-10}$	Gladstone *et al.* 1996
7	$2CH_3 + M \rightarrow C_2H_6 + M$	$k_0 = 8.76 \times 10^{-7}\ e^{-1390/T}\ T^{-7.0}$ $k_\infty = 1.4 \times 10^{-9}\ e^{-329/T}$	Gladstone *et al.* 1996
8	$CH_3 + C_2H_3 + M \rightarrow C_3H_6 + M$	$k_0 = 1.3 \times 10^{-22}$ $k_\infty = 9.1 \times 10^{-12}$	Yung *et al.* 1984
9	$CH_3 + C_2H_5 + M \rightarrow C_3H_8 + M$	$k_0 = 1.0 \times 10^{-22}\ e^{341/T}$ $k_\infty = 8.1 \times 10^{-11}$	Gladstone *et al.* 1996
10	$C_2H + H + M \rightarrow C_2H_2 + M$	$k_0 = 1.3 \times 10^{-18}\ e^{-721/T}\ T^{-3.1}$ $k_\infty = 3.0 \times 10^{-10}$	Tsang *et al.* 1986
11	$C_2H_2 + H + M \rightarrow C_2H_3 + M$	$k_0 = 6.4 \times 10^{-25}\ e^{-1200/T}\ T^{-2.0}$ $k_\infty = 3.8 \times 10^{-11}\ e^{-1374/T}$	Gladstone *et al.* 1996
12	$C_2H_4 + H + M \rightarrow C_2H_5 + M$	$k_0 = 2.15 \times 10^{-29}\ e^{-349/T}$ $k_\infty = 4.4 \times 10^{-11}\ e^{-1087/T}$	Gladstone *et al.* 1996
13	$2C_2H_5 + M \rightarrow C_4H_{10} + M$	$k_0 = 1.55 \times 10^{-22}\ e^{586/T}$ $k_\infty = 1.4 \times 10^{-11}\ e^{35.2/T}$	Gladstone *et al.* 1996
14	$C_3H_2 + H + M \rightarrow C_3H_3 + M$	$k_0 = 6.33 \times 10^{-29}\ e^{-20/T}$ $k_\infty = 3.0 \times 10^{-10}$	Toublanc *et al.* 1995
15	$C_3H_3 + H + M \rightarrow CH_3CCH + M$	$k_0 = 6.33 \times 10^{-29}\ e^{-20/T}$ $k_\infty = 3.0 \times 10^{-10}$	Toublanc *et al.* 1995
16	$C_3H_3 + H + M \rightarrow CH_2CCH_2 + M$	$k_0 = 6.33 \times 10^{-29}\ e^{-20/T}$ $k_\infty = 3.0 \times 10^{-10}$	Toublanc *et al.* 1995
17	$CH_2CCH_2 + H + M \rightarrow CH_3 + C_2H_2 + M$	$k_0 = 8.0 \times 10^{-24}\ e^{-1225/T}\ T^{-2.0}$ $k_\infty = 9.7 \times 10^{-12}\ e^{-1550/T}$	Toublanc *et al.* 1995
18	$CH_2CCH_2 + H + M \rightarrow C_3H_5 + M$	$k_0 = 8.0 \times 10^{-24}\ e^{-1225/T}\ T^{-2.0}$ $k_\infty = 1.4 \times 10^{-11}\ e^{-1000/T}$	Toublanc *et al.* 1995
19	$CH_3CCH + H + M \rightarrow CH_3 + C_2H_2 + M$	$k_0 = 8.0 \times 10^{-24}\ e^{-1225/T}\ T^{-2.0}$ $k_\infty = 9.7 \times 10^{-12}\ e^{-1550/T}$	Toublanc *et al.* 1995
20	$CH_3CCH + H + M \rightarrow C_3H_6 + M$	$k_0 = 8.0 \times 10^{-24}\ e^{-1225/T}\ T^{-2.0}$ $k_\infty = 9.7 \times 10^{-12}\ e^{-1550/T}$	Toublanc *et al.* 1995
21	$C_3H_5 + H + M \rightarrow C_3H_6 + M$	$k_0 = 1.0 \times 10^{-28}$ $k_\infty = 1.7 \times 10^{-10}$	Gladstone *et al.* 1996
22	$C_3H_6 + H + M \rightarrow C_3H_7 + M$	$k_0 = 2.15 \times 10^{-28}\ e^{-349/T}$ $k_\infty = 2.6 \times 10^{-11}\ e^{-798/T}$	Gladstone *et al.* 1996
23	$C_4H + H + M \rightarrow C_4H_2 + M$	$k_0 = 4.2 \times 10^{-19}\ e^{-721/T}\ T^{-3.1}$ $k_\infty = 1.0 \times 10^{-10}$	Toublanc *et al.* 1995
24	$C_4H_2 + H + M \rightarrow C_4H_3 + M$	$k_0 = 4.7 \times 10^{-21}\ e^{-1184/T}\ T^{-2.0}$ $k_\infty = 1.4 \times 10^{-10}\ e^{-1184/T}$	Summers and Strobel 1989
25	$C_4H_3 + H + M \rightarrow C_4H_4 + M$	$k_0 = 4.7 \times 10^{-21}\ e^{-1184/T}\ T^{-2.0}$ $k_\infty = 1.4 \times 10^{-10}\ e^{-1184/T}$	Summers and Strobel 1989
26	$C_3H_7 + CH_3 + M \rightarrow C_4H_{10} + M$	$k_0 = 2.5 \times 10^{-19}$ $k_\infty = 4.2 \times 10^{-11}\ e^{-200/T}$	Yung *et al.* 1984

[a] Units: k_0, (cm^6/s); k_∞, (cm^3/s).

TABLE IV
Bimolecular Chemical Reactions

	Reaction	Rate coefficient (cm^3/s)	Reference
1	$CH + CH_4 \rightarrow C_2H_4 + H$	$5.0 \times 10^{-11}\, e^{200/T}$	Toublanc *et al.* 1995
2	$CH + C_2H_2 \rightarrow C_3H_2 + H$	$3.49 \times 10^{-10}\, e^{61/T}$	Gladstone *et al.* 1996
3	$CH + C_2H_4 \rightarrow CH_2CCH_2 + H$	$2.23 \times 10^{-10}\, e^{173/T}$	Gladstone *et al.* 1996
4	$CH + C_2H_6 \rightarrow C_3H_6 + H$	$1.8 \times 10^{-10}\, e^{132/T}$	Gladstone *et al.* 1996
5	$^1CH_2 + H_2 \rightarrow {}^3CH_2 + H_2$	1.26×10^{-11}	Gladstone *et al.* 1996
6	$^1CH_2 + H_2 \rightarrow CH_3 + H$	9.2×10^{-11}	Gladstone *et al.* 1996
7	$^1CH_2 + CH_4 \rightarrow {}^3CH_2 + CH_4$	1.2×10^{-11}	Gladstone *et al.* 1996
8	$^1CH_2 + CH_4 \rightarrow 2CH_3$	5.9×10^{-11}	Gladstone *et al.* 1996
9	$^1CH_2 + N_2 \rightarrow {}^3CH_2 + N_2$	7.9×10^{-12}	Yung *et al.* 1984
10	$^3CH_2 + H \rightarrow CH + H_2$	$4.7 \times 10^{-10}\, e^{-370/T}$	Gladstone *et al.* 1996
11	$^3CH_2 + CH_3 \rightarrow C_2H_4 + H$	7.0×10^{-11}	Gladstone *et al.* 1996
12	$^3CH_2 + {}^3CH_2 \rightarrow C_2H_2 + 2H$	$2.1 \times 10^{-10}\, e^{-408/T}$	Gladstone *et al.* 1996
13	$^3CH_2 + C_2H_5 \rightarrow C_2H_4 + CH_3$	3.0×10^{-11}	Gladstone *et al.* 1996
14	$CH_3 + C_2H_3 \rightarrow C_2H_2 + CH_4$	3.4×10^{-11}	Toublanc *et al.* 1995
15	$CH_3 + C_2H_5 \rightarrow C_2H_4 + CH_4$	4.7×10^{-12}	Gladstone *et al.* 1996
16	$C_2 + CH_4 \rightarrow C_2H + CH_3$	$5.1 \times 10^{-11}\, e^{-297/T}$	Gladstone *et al.* 1996
17	$C_2 + H_2 \rightarrow C_2H + H$	$1.77 \times 10^{-10}\, e^{-1469/T}$	Gladstone *et al.* 1996
18	$C_2H + CH_4 \rightarrow C_2H_2 + CH_3$	$9.0 \times 10^{-12}\, e^{-250/T}$	Gladstone *et al.* 1996
19	$C_2H + C_2H_2 \rightarrow C_4H_2 + H$	1.5×10^{-10}	Gladstone *et al.* 1996
20	$C_2H + C_2H_4 \rightarrow C_4H_4 + H$	2.5×10^{-11}	Toublanc *et al.* 1995
21	$C_2H + C_2H_6 \rightarrow C_2H_2 + C_2H_5$	3.62×10^{-11}	Gladstone *et al.* 1996
22	$C_2H + C_3H_8 \rightarrow C_2H_2 + C_3H_7$	6.0×10^{-12}	Toublanc *et al.* 1995
23	$C_2H + C_4H_2 \rightarrow C_6H_2 + H$	4.15×10^{-11}	Toublanc *et al.* 1995
24	$C_2H_3 + H \rightarrow C_2H_2 + H_2$	6.0×10^{-12}	Gladstone *et al.* 1996
25	$C_2H_3 + C_2H_3 \rightarrow C_2H_4 + C_2H_2$	2.4×10^{-11}	Toublanc *et al.* 1995
26	$C_2H_3 + C_2H_5 \rightarrow C_2H_6 + C_2H_2$	8.0×10^{-13}	Gladstone *et al.* 1996
27	$C_2H_3 + C_2H_5 \rightarrow 2C_2H_4$	8.0×10^{-13}	Gladstone *et al.* 1996
28	$C_2H_5 + H \rightarrow 2CH_3$	$8.0 \times 10^{-11}\, e^{-127/T}$	Gladstone *et al.* 1996
29	$C_2H_5 + H \rightarrow C_2H_4 + H_2$	3.0×10^{-12}	Gladstone *et al.* 1996
30	$C_2H_5 + C_2H_5 \rightarrow C_2H_6 + C_2H_4$	$1.2 \times 10^{-11}\, e^{-540/T}$	Gladstone *et al.* 1996
31	$C_3H_5 + H \rightarrow C_2H_2 + CH_4$	3.3×10^{-10}	Toublanc *et al.* 1995
32	$C_3H_5 + H \rightarrow CH_3CCH + H_2$	3.3×10^{-10}	Toublanc *et al.* 1995
33	$C_3H_5 + H \rightarrow CH_2CCH_2 + H_2$	3.0×10^{-11}	Toublanc *et al.* 1995
34	$C_3H_5 + CH_3 \rightarrow CH_3CCH + CH_4$	$1.15 \times 10^{-12}\, e^{66/T}$	Toublanc *et al.* 1995
35	$C_3H_5 + CH_3 \rightarrow CH_2CCH_2 + CH_4$	$1.15 \times 10^{-12}\, e^{66/T}$	Toublanc *et al.* 1995
36	$C_3H_7 + H \rightarrow C_3H_6 + H_2$	5.0×10^{-11}	Gladstone *et al.* 1996
37	$C_3H_7 + H \rightarrow C_2H_5 + CH_3$	6.0×10^{-11}	Gladstone *et al.* 1996
38	$C_3H_7 + CH_3 \rightarrow C_3H_6 + CH_4$	$1.85 \times 10^{-12}\, e^{339/T}$	Toublanc *et al.* 1995
39	$C_4H + CH_4 \rightarrow C_4H_2 + CH_3$	$9.3 \times 10^{-13}\, e^{-250/T}$	Yung *et al.* 1984
40	$C_4H + C_2H_2 \rightarrow C_6H_2 + H$	1.0×10^{-11}	Yung *et al.* 1984
41	$C_4H + C_2H_4 \rightarrow C_4H_2 + C_2H_3$	1.2×10^{-11}	Toublanc *et al.* 1995
42	$C_4H + C_2H_6 \rightarrow C_4H_2 + C_2H_5$	2.1×10^{-11}	Gladstone *et al.* 1996
43	$C_4H + C_4H_2 \rightarrow C_8H_2 + H$	5.81×10^{-11}	Toublanc *et al.* 1995
44	$C_4H_2{}^{**} + N_2 \rightarrow C_4H_2 + N_2$	1.0×10^{-11}	Summers and Strobel 1989
45	$C_4H_2{}^{**} + C_2H_2 \rightarrow C_6H_2 + H_2$	1.0×10^{-11}	Summers and Strobel 1989
46	$C_4H_2{}^{**} + C_4H_2 \rightarrow C_8H_2 + H_2$	1.0×10^{-11}	Summers and Strobel 1989
47	$C_4H_3 + H \rightarrow 2C_2H_2$	3.3×10^{-12}	Gladstone *et al.* 1996
48	$C_4H_3 + H \rightarrow C_4H_2 + H_2$	1.2×10^{-11}	Yung *et al.* 1984
49	$CH_2CCH_2 + H \rightarrow CH_3CCH + H$	$1.0 \times 10^{-11}\, e^{-1000/T}$	Gladstone *et al.* 1996

The five primitive equations are used to derive the partial differential equation for the meridional circulation,

$$-\frac{2\tan\phi}{a}\left(\hat{f}\bar{v}^* - \frac{\partial\bar{u}}{\partial z}\bar{w}^*\right)\frac{\partial\bar{u}}{\partial z} - \tilde{f}\frac{\partial}{\partial z}(\hat{f}\bar{v}^*) + \tilde{f}\frac{\partial}{\partial z}\left(\bar{w}^*\frac{\partial\bar{u}}{\partial y}\right) + R^*\frac{\partial}{\partial y}\left(\bar{v}^*\frac{\partial\bar{\theta}}{\partial y}\right) + R^*\frac{\partial}{\partial y}(\hat{S}\bar{w}^*) = F_1, \tag{17}$$

where

$$\hat{f} \equiv f - \frac{1}{a\cos\phi}\frac{\partial}{\partial\phi}(\bar{u}\cos\phi), \tag{18}$$

$$\tilde{f} \equiv f + \frac{2\tan\phi}{a}\bar{u}, \tag{19}$$

$$R^* \equiv \frac{R}{H_0}\exp\left(-\frac{\kappa z}{H_0}\right), \tag{20}$$

TABLE V
Parameters and Variables Used in the Dynamics Equations

a	equatorial radius of Titan's tropopause
z	log pressure altitude $\equiv -H_0 \ln(P/P_0)$
ϕ	latitude
H_0	reference scale height $\equiv 30$ km
R	gas constant
k	Boltzmann's constant
P	pressure
P_0	reference pressure, tropopause pressure ≈ 144 mb
ρ_0	horizontally averaged density $\equiv \rho_s \exp(-z/H_0)$, $\rho_s \equiv$ reference density
u	zonal velocity, positive in the direction of rotation
v	meridional velocity, positive toward the north
w	vertical velocity, positive up
Φ	geopotential
C_p	specific heat at constant pressure
κ	ratio of gas constant to specific heat, $\equiv R/C_p$
T	temperature
θ	potential temperature
Ω	rotation rate of Titan
f	Coriolis parameter
Q	heating rate
G	zonally averaged eddy flux of heat term
τ_r	radiative time constant
τ_f	Rayleigh friction time constant
X	non-conservative force component in the zonal direction, F_{fr_λ}
Y	non-conservative force component in meridional direction, F_{fr_ϕ}
ψ	streamfunction
F	Eliassen–Palm flux

and the static stability, $\hat{S}$, is used to approximate the vertical derivative of the mean potential temperature,

$$\hat{S} \approx \frac{\partial \bar{\theta}}{\partial z}. \tag{21}$$

The forcing term on the right-hand side of Eq. (17) is expressed in terms of mechanical forcing, M, and thermal forcing J as given by

$$F_1 = \tilde{f}\frac{\partial M}{\partial z} + \frac{2\tan\phi}{a} M \frac{\partial \bar{u}}{\partial z} + R^* \frac{\partial J}{\partial y}, \tag{22}$$

where

$$M \equiv \frac{1}{\rho_0 a \cos\phi} \nabla \cdot \mathbf{F} + \bar{X}, \tag{23}$$

and

$$J \equiv \bar{Q} - \frac{1}{\rho_0}\left[\frac{1}{a}\frac{\partial}{\partial z}\left(\rho_0 \frac{\overline{v'\theta'}}{(\partial\bar{\theta}/\partial z)}\frac{\partial\bar{\theta}}{\partial\phi}\right) + \frac{\partial}{\partial z}(\rho_0 \overline{w'\theta'})\right]. \tag{24}$$

Let

$$\bar{v}^* \equiv -\frac{1}{\cos\phi}\left(\frac{\partial\psi}{\partial z} - \frac{\psi}{H_0}\right) \quad \text{and} \quad \bar{w}^* \equiv \frac{1}{\cos\phi}\frac{\partial\psi}{\partial y} \tag{25a,b}$$

define the streamfunction. Equation (17) can now be written as

$$C_{11}\frac{\partial^2\psi}{\partial y^2} + C_{12}\frac{\partial^2\psi}{\partial y\partial z} + C_{22}\frac{\partial^2\psi}{\partial z^2} + C_1\frac{\partial\psi}{\partial y} + C_2\frac{\partial\psi}{\partial z} + C_0\psi = F, \tag{26}$$

where

$$C_{11} \equiv R^*\hat{S}, \quad C_{12} \equiv \tilde{f}\frac{\partial\bar{u}}{\partial z} - R^*\frac{\partial\bar{\theta}}{\partial y}, \quad C_{22} \equiv \hat{f}\tilde{f} \tag{27a,b,c}$$

$$C_1 \equiv \tilde{f}\frac{\partial^2\bar{u}}{\partial^2 z} + R^*\left(\frac{\partial^2\bar{\theta}}{\partial y\partial z} + \frac{1}{H_0}\frac{\partial\bar{\theta}}{\partial y}\right) + \frac{\tan\phi}{a}\left[2\left(\frac{\partial\bar{u}}{\partial z}\right)^2 + R^*\hat{S}\right] \tag{28}$$

$$C_2 \equiv \frac{\partial\bar{u}}{\partial z}\left[\frac{\partial\tilde{f}}{\partial y} + \frac{2\tan\phi}{a}(\hat{f}+\tilde{f})\right] - \frac{\hat{f}\tilde{f}}{H_0} \tag{29}$$

$$C_0 \equiv -\frac{1}{H_0}\frac{\partial\bar{u}}{\partial z}\left[\frac{\partial\tilde{f}}{\partial y} + \frac{2\tan\phi}{a}(\hat{f}+\tilde{f})\right] \tag{30}$$

and

$$F \equiv F_1 \cos\phi. \tag{32}$$

On a numerical grid, Eq. (26) is solved using a 7-point finite difference scheme. The finite difference form of Eq. (26) is

$$A_x\psi_{J+1,K} + C_x\psi_{J-1,K} + A_y\psi_{J,K+1} + C_y\psi_{J,K-1} + B_0\psi_{J,K} + A_z\psi_{J-1,K-1} + C_z\psi_{J+1,K+1} = F_{J,K}. \tag{33}$$

where $\Delta_y \equiv a\Delta\phi$. The array coefficients are defined by

$$\begin{aligned}
A_x &= \left(\frac{C_{11}}{\Delta y^2} - \frac{C_{12}}{2\Delta y\Delta z} + \frac{C_1}{2\Delta y}\right)\\
A_y &= \left(-\frac{C_{12}}{2\Delta y\Delta z} + \frac{C_{22}}{\Delta z^2} + \frac{C_2}{2\Delta z}\right)\\
C_x &= \left(\frac{C_{11}}{\Delta y^2} - \frac{C_{12}}{2\Delta y\Delta z} - \frac{C_1}{2\Delta y}\right)\\
C_y &= \left(-\frac{C_{12}}{2\Delta y\Delta z} + \frac{C_{22}}{\Delta z^2} - \frac{C_2}{2\Delta z}\right)\\
B_0 &= \left(-\frac{2C_{11}}{\Delta y^2} - \frac{2C_{22}}{\Delta z^2} + \frac{C_{12}}{\Delta y\Delta z} + C_0\right)\\
A_z &= C_z = \left(\frac{C_{12}}{2\Delta y\Delta z}\right).
\end{aligned} \tag{34}$$

Equation (33) is solved using the Gauss–Siedel method (Press *et al.* 1989). The boundary conditions assume zero meridional velocities at each pole and zero vertical velocities at the upper and lower boundaries, similar to Hutzell *et al.* (1996). The para

meters A_x, A_y, A_z, C_x, C_y, C_z, B_0, and $F_{J,K}$ are evaluated at all points (J, K) for each time step.

For simplicity in this model, the mechanical forcing will only be expressed in terms of eddy and Rayleigh friction. These forces are parameterized using

$$M = \frac{1}{\rho}\frac{\partial}{\partial z}\left(\rho K_{zz}\frac{\partial \bar{u}}{\partial z}\right) - \frac{\bar{u}}{\tau_f}. \tag{35}$$

Here K_{zz} is the eddy diffusion coefficient and τ_f the Rayleigh frictional damping time constant. Both K_{zz} and τ_f are free parameters in this model. Typically, in 1-D photochemical transport models, K_{zz} is adjusted until the results match the steady-state number density of a particular species whose abundance is well known. This work borrows the results from 1-D models to constrain the values for K_{zz}.

For computational simplicity, Newtonian cooling is used to model the net heating rate,

$$Q = \alpha_r\left(\bar{\theta} - \langle\bar{\theta}\rangle\right) = \frac{\bar{\theta} - \langle\bar{\theta}\rangle}{\tau_r}. \tag{36}$$

Here, α_r is the Newtonian cooling coefficient, equal to the reciprocal of the radiative time constant, τ_r. The brackets in Eq. (36) imply a meridional mean. Frictional damping constants for the stratospheres of planets are typically within an order of magnitude of the radiative time constants (McMillan 1992). Therefore, in this model the approximation $\tau_f = \tau_r$ is employed.

The eddy terms from Eq. (24) can be expressed using mixing length theory,

$$\begin{aligned}\frac{\partial}{\partial z}&\left(\rho_0\frac{\overline{v'\theta'}}{(\partial\bar{\theta}/\partial z)}\frac{\partial\bar{\theta}}{\partial y}\right) + \frac{\partial}{\partial z}(\rho_0\overline{w'\theta'}) \\ &= \frac{\partial}{\partial z}\left(\frac{\rho_0}{\langle\partial\bar{\theta}/\partial z\rangle + (\partial\bar{\theta}/\partial z)}\left[K_{yy}\left(\frac{\partial\bar{\theta}}{\partial y}\right)^2\right.\right. \\ &\quad \left.\left. + K_{zz}\left(\left\langle\frac{\partial\bar{\theta}}{\partial z}\right\rangle + \frac{\partial\bar{\theta}}{\partial z}\right)^2\right]\right),\end{aligned} \tag{37}$$

where the Ks are the eddy diffusion tensor components. Thus, the overall thermal forcing becomes

$$\begin{aligned}J = \frac{\bar{\theta} - \langle\bar{\theta}\rangle}{\tau_r} &+ \frac{1}{\rho_0}\frac{\partial}{\partial z}\left(\frac{\rho_0}{\langle\partial\bar{\theta}/\partial z\rangle + (\partial\bar{\theta}/\partial z)}\left[K_{yy}\left(\frac{\partial\bar{\theta}}{\partial y}\right)^2\right.\right. \\ &\left.\left. + K_{zz}\left(\left\langle\frac{\partial\bar{\theta}}{\partial z}\right\rangle + \frac{\partial\bar{\theta}}{\partial z}\right)^2\right]\right).\end{aligned} \tag{38}$$

Now that the forcing terms have been parameterized, all that is needed to solve the dynamical equations are the seasonal temperature fields and estimates for the eddy diffusion coefficients and radiative time constants. The zonal winds are calculated using the thermal wind equation. The grid spacing must be set so that there are no grid lines at or close to the equator, or at the poles, where the dynamical equations are not valid.

5. ADVECTIVE AND DIFFUSIVE TRANSPORT

In 1-D photochemical models, eddy and molecular diffusion are the only processes considered in the transport of molecular species. For 2-D photochemical models, advection becomes a major part of the tracer transport. On Earth, where orographic and planetary vorticity effects are prevalent, planetary waves are responsible for strong meridional tracer transport. The Earth's fast rotation is responsible for this planetary vorticity. On a slowly rotating body such as Titan, planetary vorticity effects are not expected. Therefore, advection is the dominant mode of meridional tracer transport and meridional diffusive transport can be neglected entirely.

Once the meridional velocity field is determined, the advection, Eq. (4), can be solved. This work uses the conservation of second-order moments advection algorithm developed by Prather (1986), modified for spherical coordinates. For each time step, the Prather method not only conserves the total tracer abundance (the zeroeth-order moments) but also conserves the mean slope of the tracer distribution in each dimension (first-order moments) and the curvature in the tracer distribution, including cross terms (second-order moments). An advantage of the Prather method is that time steps can be used all the way up to the Courant limit. The Courant limit is reached when all the contents of a grid cell are transported in one time step. Additionally, the Prather method can maintain positive concentrations without introduction of numerical diffusion and can resolve tracer gradients on the order of the grid size. A detailed discussion of this method can be found in Shia *et al.* (1990).

Finally, the diffusion equation, Eq. (5), must be solved. In spherical coordinates this equation becomes

$$\frac{\partial n_i}{\partial t} = -\frac{1}{r^2}\frac{\partial}{\partial r}(r^2\phi_i), \tag{39}$$

where

$$\phi_i = -(D_i + K_{zz})\left[\frac{\partial n_i}{\partial r} + \frac{n_i}{T}\frac{\partial T}{\partial r}\right] - \left(\frac{D_i}{H_i} + \frac{K_{zz}}{H_0}\right)n_i. \tag{40}$$

In Eqs. (39) and (40), $n_i \equiv \mu_i N$ is the number density, H_i the scale height, and D_i the diffusion coefficient of the ith constituent. All other terms have previously been defined. Equation (39) is solved using a time-dependent, implicit, centered finite-difference algorithm.

Lower boundary conditions are treated in the same manner as in Yung *et al.* (1984). Upper boundary conditions are as follows. For short-lived chemical spiecies, chemical equilibrium is assumed. For the remaining hydrocarbons, it is assumed that the diffusive flux through the upper boundary is balanced by the integrated net production of that species above the upper boundary. Only atomic and molecular hydrogen are assumed to undergo Jeans escape. For these two species, the diffusive flux through

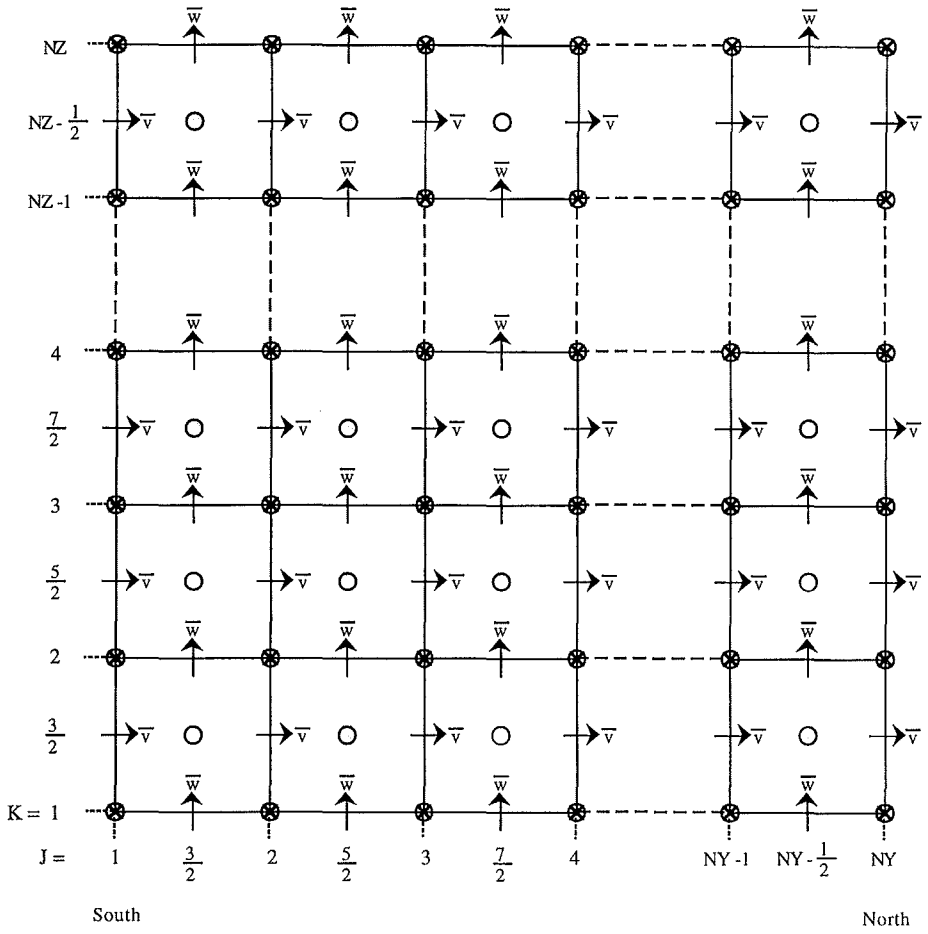

FIG. 1. Schematic representation of the grid used for the numerical model. There are $NY \times NZ$ grid points and $(NY\text{-}1) \times (NZ\text{-}1)$ cells. The number density is evaluated at the center of each cell (i.e., at $(J, K) = (3/2, 3/2)$, etc.). The vertical velocity component is calculated at the bottom of each cell ($(J, K) = (3/2, 1)$, etc.). The meridional velocity component is calculated at the left side of each cell ($(J, K) = (1, 3/2)$, etc.). The stream function is calculated at each grid point (J, K). The curvature of the atmosphere is not shown in this representation.

the upper boundary is fixed by the integrated net production and the Jeans escape flux at the exobase.

6. THE TWO-DIMENSIONAL MODEL

The grid structure used for Titan's stratosphere is characterized in Fig. 1. In the meridional direction the grid points were restricted to the latitude range (−85°, +85°). Latitude bins of 10° width were used, as they sufficiently resolved the meridional structure. The lower boundary, $z = 0$ in log pressure coordinates, is set at the tropopause, ≈40 km in real altitude. The upper boundary is set high in the stratosphere at 0.05 mbar pressure. The upper boundary is at 240 km in log pressure coordinates, corresponding to a real altitude of ~300 km. This upper boundary allows at least two scale heights above the altitudes where the weighting functions for the chemical species of interest peak (Coustenis *et al.* 1989, 1991, 1995). Equally important, this altitude range yields an atmospheric layer that is thin compared to the radius of the satellite, justifying the approximations made in the dynamical equations.

Because the density of the atmosphere decreases exponentially with altitude, the vertical resolution in the numerical model must be smaller than the scale height. A general rule of thumb for numerical resolution of an exponential is $\Delta z < H/3$. The minimum scale height in the region of interest occurs at the tropopause, where the minimum stratosphere temperature occurs. The scale height at the tropopause is approximately 15 km. Using $NZ = 60$ results in $\Delta z = 4.0$ km. This is sufficient to resolve the exponential pressure relationship and gives an 18×61 grid overall.

Radiative time constants, eddy diffusion coefficients, temperatures, and zonal wind velocities are required inputs for the model to perform chemical, dynamical, and diffusive transport calculations. Radiative time constants for Titan's atmosphere were estimated by Flasar *et al.* (1981). These are shown in Fig. 2a. A simple least-quares fit of this data is used in this model. The eddy diffusion coefficient is modeled after Strobel *et al.* (1992). Figure 2b shows the model eddy diffusion coefficients compared to those used in the 1-D photochemical models of Yung *et al.* (1984) and Toublanc *et al.* (1995).

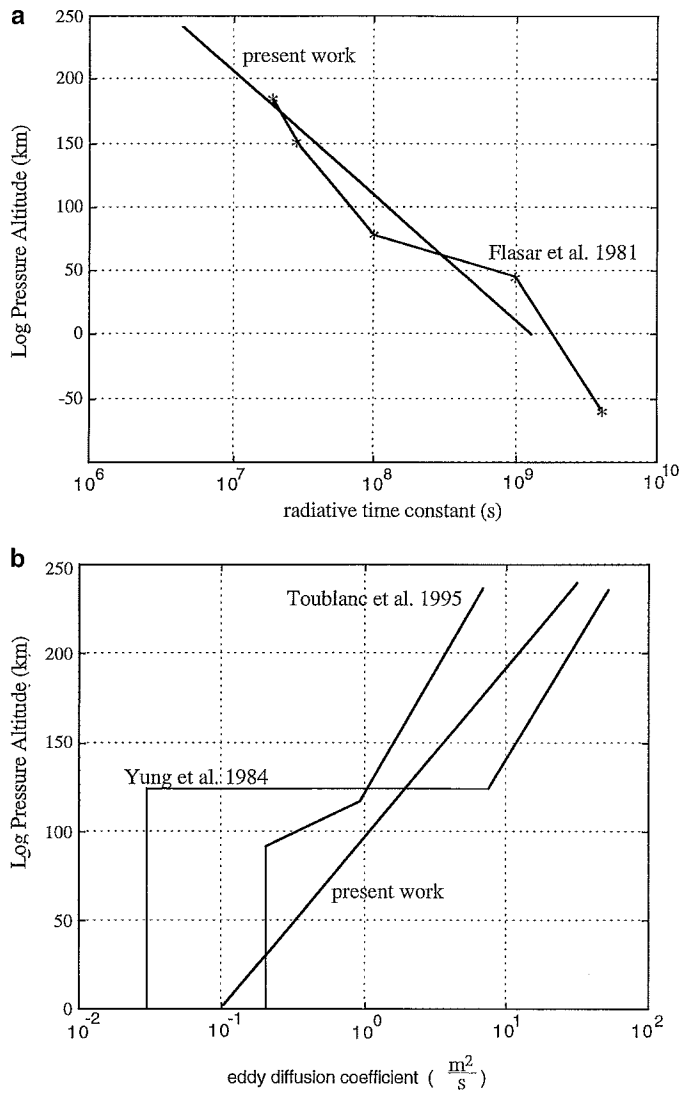

FIG. 2. (a) Radiative time constants for Titan's stratosphere. (b) Eddy diffusion coefficients for Titan's stratosphere. In log pressure coordinates $z = 0$ corresponds to the tropopause.

Seasonal temperature profiles are modeled after Hourdin *et al.* (1995). They used an intensive radiative transfer model coupled with a GCM to generate solstice and equinox temperature fields. Their vertical temperature structure was modeled after Lellouch *et al.* (1989). Yelle (1991) showed a slight decrease in stratosphere temperatures above 1 mbar not incorporated into the model of Hourdin *et al.* In this work we empirically fit Hourdin *et al.*'s temperatures fields for Northen Hemisphere winter solstice and vernal equinox. We assume the temperature fields were reversed, symmetric around the equator for the summer solstice and autumnal equinox. Corrections were made for temperatures above 1 mbar to be consistent with the findings of Yelle (1991). Figure 3 shows the temperature profiles for equinox and solstice.

All numerical modeling to solve Eq. (1) is coded in FORTRAN 77 and run on a DEC 3000 VMS Workstation. The time step is 10^6 s, the maximum time step possible without exceeding the Courant limit during numerical advection. A time step starts out by calculating the subsolar latitude. The subsolar latitude is then used as input to determine the temperature field and photolysis rates for each grid cell. Photolysis, chemical, and sublimation reactions are used to calculate the production and loss of each chemical species in each grid cell for the present time step. Molecular diffusion coefficients are determined from the temperature field. Diffusive and eddy transport calculations are then conducted. Finally, the velocity field is determined and advective transport calculations are performed.

Initial number densities for all latitudes are assigned by using the values calculated from the Yung *et al.* model. This assignment generally underestimates the abundance of hydrocarbons near the equator and overestimates their abundances near the poles. However, these initial guesses are found to always lead to convergence. The mixing ratio for CH_4 is held at 0.02 at the

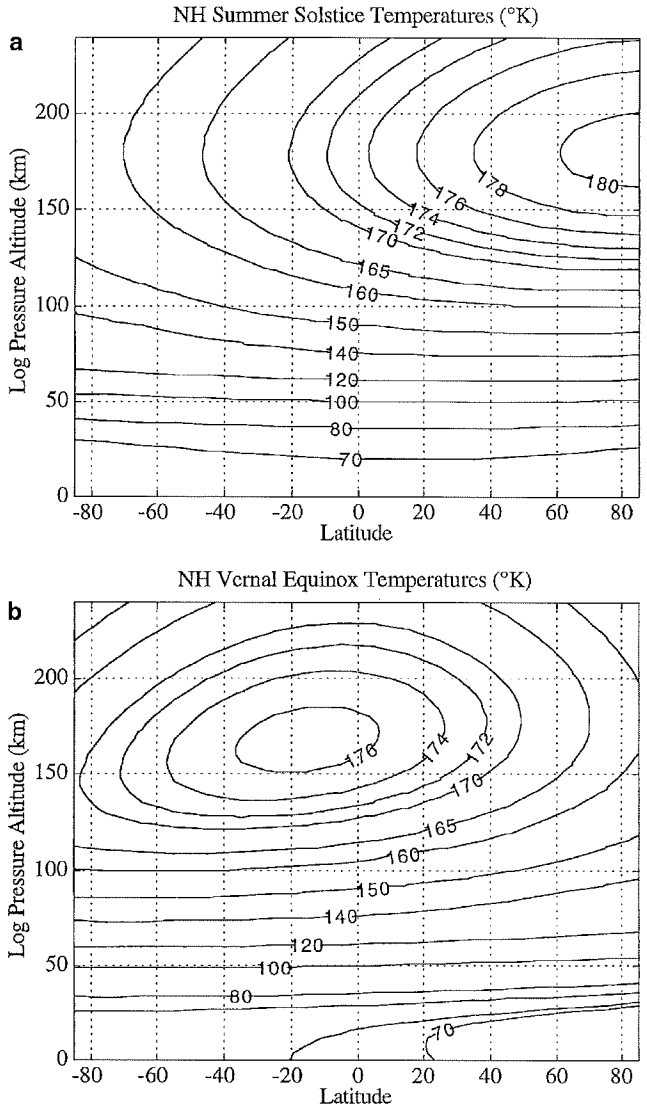

FIG. 3. Model temperature fields for (a) solstice and (b) equinox.

tropopause, resulting in the same mixing ratio throughout the stratosphere. Short-lived chemical species are not transported, saving valuable CPU time.

Since this is a time-dependent model, the number density of each species does not converge to a definite value in each grid cell. Instead, the number density of each species converges to a repeatable seasonal cycle. For a typical run of the code all species reach steady state in approximately 100,000 iterations (~107 equivalent Titan years) using approximately 100 h of CPU time.

7. MODEL RESULTS

Since CH_4 is well mixed in Titan's stratosphere, C_2H_6 is used to constrain the values for the forcing parameters. Figure 4a shows the meridional distribution of C_2H_6 from the nominal model for northern vernal equinox. As seen in the figure, there is a marked equator-to-pole increase in C_2H_6 abundance in both hemispheres. To begin to understand the cause for the high latitude abundance enhancement, Fig. 4a should be compared to Fig. 4b. The data plotted in Fig. 4b are from a run of the code with the exact same conditions as those producing Fig. 4a, except that advection is turned off. Shutting off the advection essentially gives a one-dimensional photochemical model at each latitude, where the solar zenith angle and temperature field are allowed to vary with the seasons. In Fig. 4b the equator has the highest abundance of ethane, the opposite of what is seen in Fig. 4a. With no meridional transport, one would expect more ethane near the equator than near the poles, since more photolysis occurs annually near the equator than near the poles. It can be concluded that advective transport is responsible for differences seen between Figs. 4a and 4b. Physically, the average annual vertical velocities are positive at low latitudes (Hourdin *et al.*). The upward advective flux of ethane dominates the downward diffusive flux of ethane that is created high in the stratosphere. The result is that, instead of ethane produced near the equator being transported downward, it is advected horizontally where it collects at the poles. At the poles, the direction of the vertical velocity is upward for one season and downward for three seasons [Hourdin *et al.*], thus allowing downward diffusive transport to compete with vertical advective transport on an annual basis.

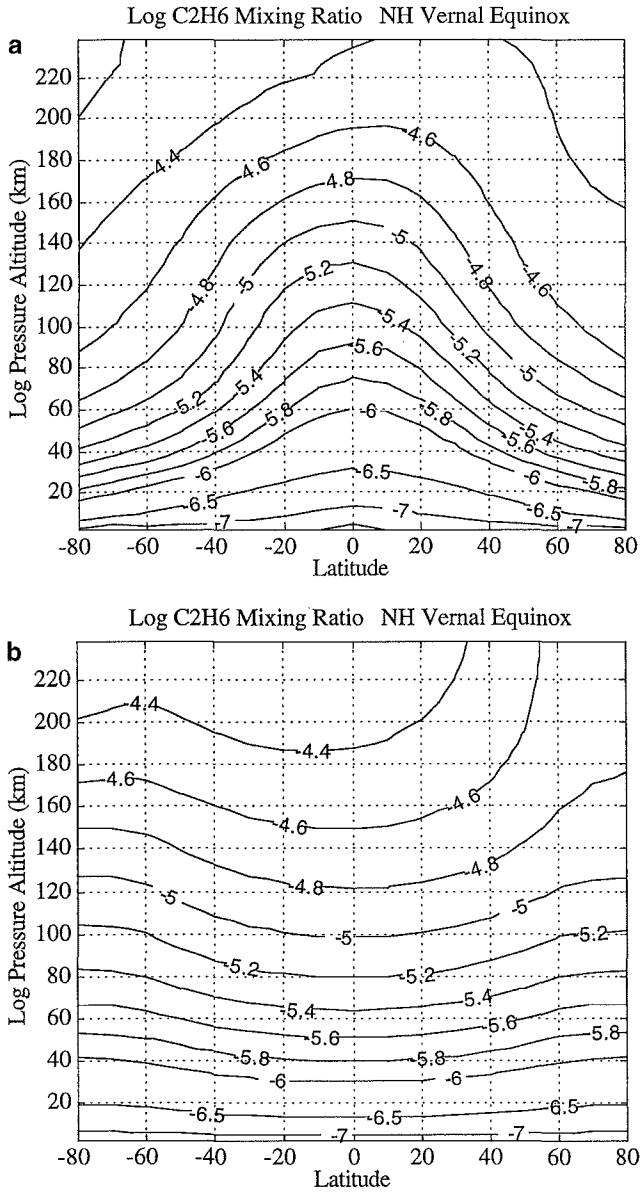

FIG. 4. Ethane abundances in Titan's stratosphere. (a) Full 2-D model with advection. (b) 2-D model with no advective transport.

The meridional ethane profile from Voyager IRIS data is much more uniform between 53°S and 30°N latitudes than that seen in Fig. 4a (Coustenis and Bézard 1995). The ethane mixing ratios plotted in Fig. 4a were calculated with a strong meridional circulation. The mixing ratios plotted in Fig. 4b were calculated using no meridional circulation. A more uniform meridional ethane distribution can only be achieved in this two-dimensional photochemical transport model if a weaker meridional circulation is used in the advection calculations.

Coustenis and Bézard (1995) report altitude data for the contribution functions only for latitudes 53°S and 50°N. Therefore, this model will only attempt to reproduce the C_2H_6 mixing ratios for the grid points closest to those latitudes for the same season. It was determined that the radiative time constant had to be increased by a factor of 10 to weaken the meridional circulation sufficiently to reproduce those results. The decrease in the radiative time constant results in the dynamical turnover time being comparable to the photochemical lifetime of ethane. Figure 5 shows that the revised profile for vernal equinox has a much more meridionally uniform C_2H_6 abundance. For the time of the Voyager 1 encounter with Titan, Fig. 6 shows that the model C_2H_6 profiles are now in close agreement with the Voyager IRIS abundances.

Figures 7–9 show mixing ratio profiles for C_2H_2, C_3H_8, and CH_3CCH, respectively. These are the three most abundant hydrocarbon species in Titan's atmosphere after CH_4 and C_2H_6. The Voyager data shown in these figures are the half-width levels for the contribution functions from Coustenis and Bézard. The results for these species all fall within the half-width altitudes.

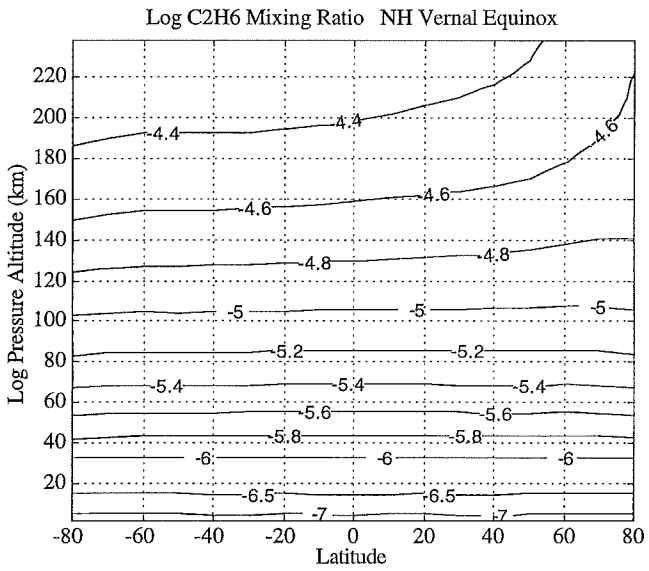

FIG. 5. Ethane abundances in Titan's stratosphere that result when the meridional circulation is weakened.

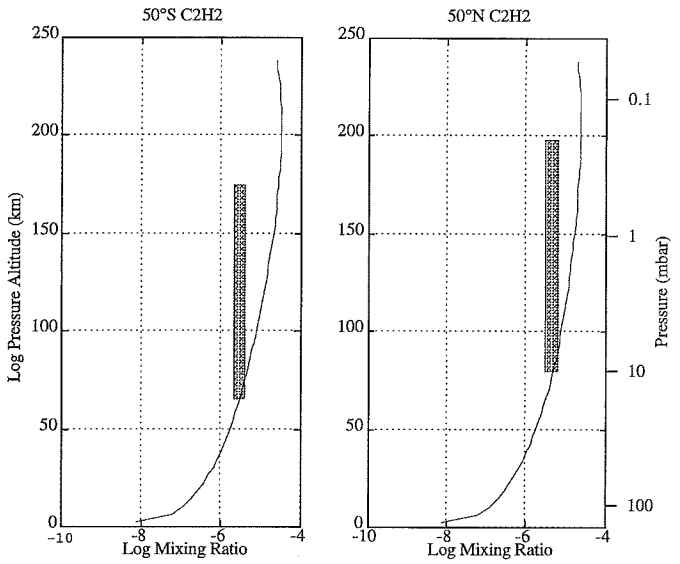

FIG. 7. Mixing ratio profiles for acetylene at latitudes 50°S and 50°N. For each latitude the model (curve) is compared to mixing ratios retrieved from Voyager IRIS data by Coustenis and Bézard (1995).

However, the model C_2H_2 mixing ratios are at the high mixing ratio extreme of the error bars, as was the case in previous 1-D models (Yung *et al.* 1984 and Lara *et al.* 1996).

Coustenis and Bézard also report an enrichment at 50°N and 70°N latitudes for some hydrocarbon species (C_2H_4, C_3H_4, and C_4H_2). Using their published altitudes for the maximum contribution functions for 53°S and 50°N, Table VI has been generated to compare the model to the observational data. Table VI shows the composition ratios, 50°N : 50°S, for these species, as well as those for C_2H_2, C_3H_8, and CH_3CCH. Recall that the strength of the meridional circulation was adjusted so that the C_2H_6 mixing ratios were in agreement with the observational data. This results in the model north–south abundance ratio for C_3H_8 being within the uncertainty from the observational data. The ratio for C_2H_2 is close to the calculated value, but as previously mentioned the model overestimates the amount of C_2H_2 (by factors of 3.8 and 2.6, respectively, for the two latitudes and altitudes in Table VI), resulting in a model ratio not exactly equal to the observed ratio.

No high-latitude enrichment is seen in the model for C_2H_4. The model overestimates the C_2H_4 abundance at 50°S by a factor of 3.5 and underestimates it by the same factor at 50°N. For C_3H_4

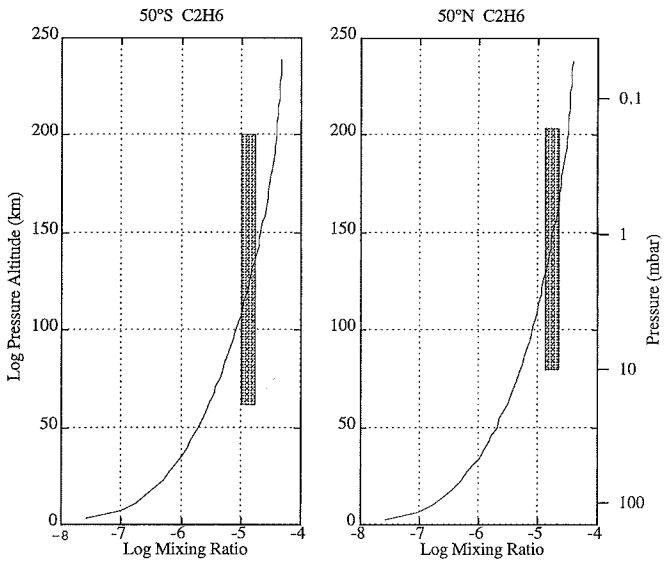

FIG. 6. Mixing ratio profiles for ethane at latitudes 50°S and 50°N. For each latitude the model (curve) is compared to mixing ratios retrieved from Voyager IRIS data by Coustenis and Bézard (1995).

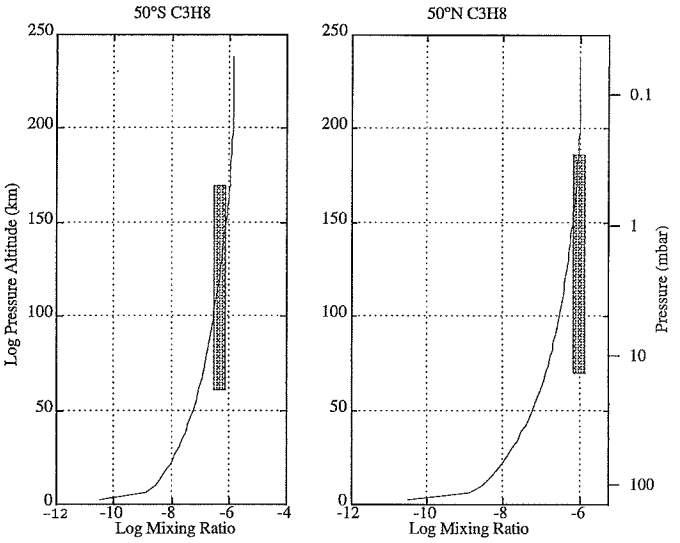

FIG. 8. Mixing ratio profiles for propane at latitudes 50°S and 50°N. For each latitude the model (curve) is compared to mixing ratios retrieved from Voyager IRIS data by Coustenis and Bézard (1995).

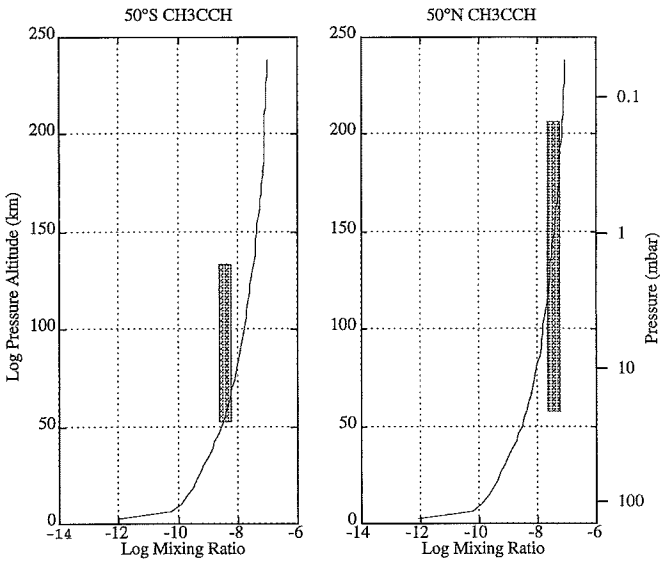

FIG. 9. Mixing ratio profiles for methylacetylene at latitudes 50°S and 50°N. For each latitude the model (curve) is compared to mixing ratios retrieved from Voyager IRIS data by Coustenis and Bézard (1995).

the model predicts a slight enrichment at 50°N over 50°S, but not an order of magnitude as observed. The smaller north–south ratio is entirely due to the model overestimating the CH_3CCH mixing ratio by a factor of 2.6 at 50°S. The model does its poorest in matching the abundances of C_4H_2. The model mixing ratio at both latitudes is overestimated by more than an order of magnitude. An enrichment is seen at 50°N over 50°S, but the north : south ratio is only 0.1 of that observed.

The seasonal variations in hydrocarbon abundances for a given latitude are shown in Fig. 10. Here, 50°N is chosen to be representative of mid-latitudes in both hemispheres. Column densities above 5 mbar are shown for C_2H_6, C_3H_8, C_2H_2, and CH_3CCH, showing how their abundances vary seasonally in the upper stratosphere. For these four species, the maximum column densities exceed the minimum values by 10, 14, 9.5, and 12%, respectively. The maximum column density for each occurs in mid-summer. This is because, although the maximum photolysis occurs at the solstice, the temperature field in the stratosphere lags behind the seasonal forcing. The maximum stratosphere

TABLE VI
Hemispheric Gas Composition Comparison

Molecule	50°S mixing ratios	50°N mixing ratios	North/south model	North/south observed[a]
C_2H_2	1.05×10^{-5}	1.46×10^{-5}	1.4	2.2 ± 0.5
C_2H_4	5.28×10^{-7}	2.86×10^{-7}	0.5	7 ± 3
C_2H_6	1.33×10^{-5}	2.39×10^{-5}	1.8	1.6 ± 0.2
CH_3CCH	1.88×10^{-9}	2.85×10^{-9}	1.5	9.5 ± 2
C_3H_8	2.11×10^{-7}	4.17×10^{-7}	2.0	1.7 ± 0.7
C_4H_2	1.81×10^{-7}	4.71×10^{-7}	2.6	23 ± 4

[a] From Table III, Coustenis and Bézard (1995).

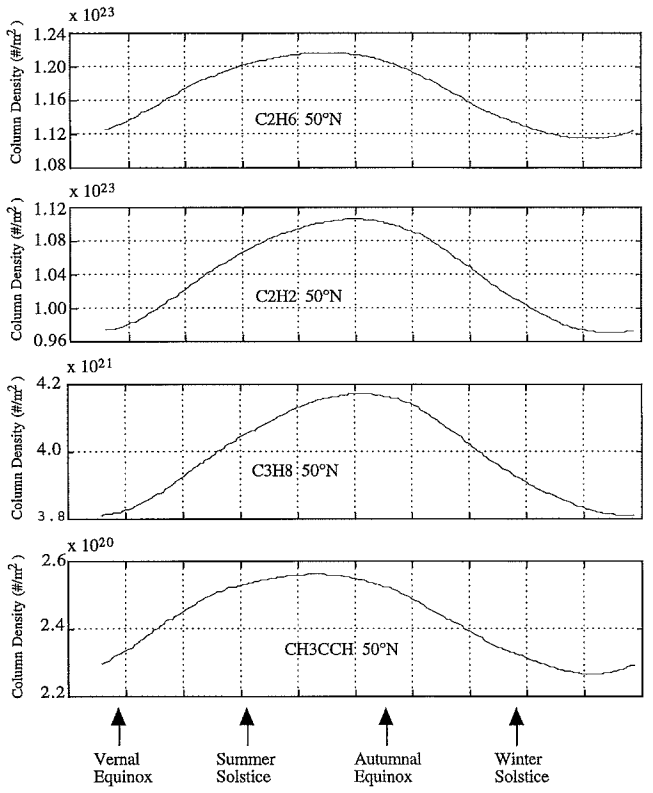

FIG. 10. Column densities above 5 mbar for C_2H_6, C_2H_2, C_3H_8, and CH_3CCH at 50°N latitude as a function of season.

temperatures occur in late summer. The peak column densities occur between the times of peak photolysis and the peak temperature, when temperature-dependent chemical reaction rates are maximum. Seasonal variations for latitudes above 50° are slightly greater than those shown in Fig. 10 while very small seasonal variations for these hydrocarbons are predicted by the model for the equator.

All chemical species more massive than C_4H_3 in this model are lumped together and called polymers. Once produced, the polymers will be photolyzed, condense, or participate in reactions to produce larger molecules. Most of the polymers are photodissociated back into smaller hydrocarbons. However, some long-chain hydrocarbons are produced and are irreversibly removed, creating the aerosol layers present in Titan's stratosphere. Heavy hydrocarbon compounds were not tracked in this photochemical model. Although the photochemical loss and condensation rates for the polymers are not calculated in this model, an upper limit for their production rate is approximated by the sum of the reaction rates of the polymer-producing reactions.

Figure 11 displays the seasonal column production rates for polymers for latitudes 0°, 20°N, 50°N, and 80°N. The production rate profiles for southern hemisphere latitudes would be analogous to the northern hemisphere latitudes displayed in this figure. In Fig. 11, the column production rates for equatorial latitudes (0°–20°) are fairly constant throughout the year. At 50°N,

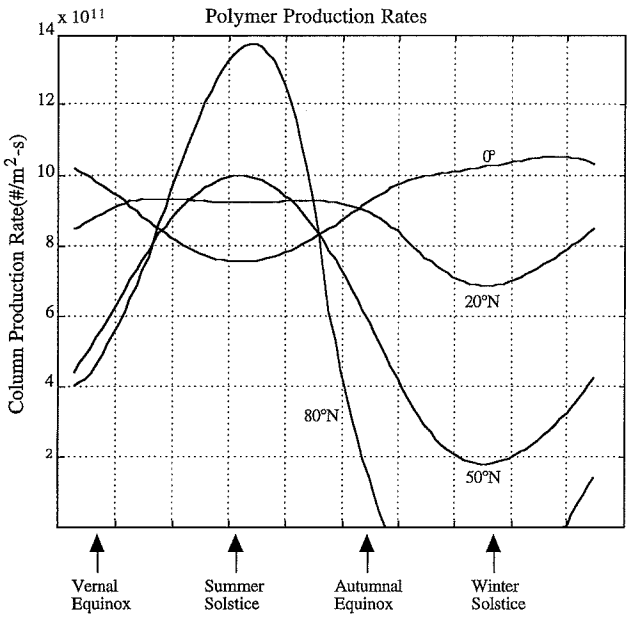

FIG. 11. Column production rates of polymers in Titan's stratosphere as a function of season.

the production rate in the summer peaks at a value 5 times greater than the minimum production rate in the winter. The extrema in production rates occur at polar latitudes, where the production rate in the summer is 25% greater than the production rate at 50°N and 40% greater than at the equator. During the polar winter, the production of polymers ceases altogether as the supply of free radicals ends due to the absence of sunlight.

8. DISCUSSION

The coupling of dynamics, thereby advection, photochemistry, and diffusion in two-dimensional photochemical models makes it difficult to determine which parameters need adjustment to accurately match observational data. Changes in any dynamical parameter, chemical reaction rate, or boundary condition can notably change the overall seasonal distribution of most of the chemical species. This work attempted to simplify the problem by limiting the vertical extent of the region of interest, the number of chemical species, and the number of chemical reactions.

The vertical region of interest, from the tropopause to 0.05 mbar, may appear to be well below where most of the CH_4 photolysis occurs. However, this region of Titan's atmosphere is dominated by photosensitized destruction of CH_4 (Yung *et al.* 1984). The photosensitized destruction of CH_4 is brought about by the photolysis of C_2H_2 and C_4H_2, both of which are as readily photolyzed in this region as they are higher in the atmosphere. Therefore, the model mole fractions of C_2H_6 and C_3H_8, the two most abundant hydrocarbons after CH_4 and the two major products of CH_4 destruction, produced in this region of the atmosphere should be accurate. When the strength of the model meridional circulation is adjusted to match the observed ethane abundances for 50°S and 50°N latitudes, the results for both C_2H_6 and C_3H_8 are quite satisfactory.

For CH_3CCH, the model is fairly accurate in matching the observed abundances at 50°N; however, as previously mentioned, the model abundance is high at 50°S, resulting in a smaller north–south ratio than what was observed. However, the model comes closer to the observed abundances than previous 1-D models (Yung *et al.* 1984, Toublance *et al.* 1995, and Lara *et al.* 1996).

A serious shortcoming of the model is the failure to more closely match C_2H_2 with the Voyager data. Model values for 50°S and 50°N are high by factors of 3.8 and 2.6, respectively. Model abundances for C_4H_2 are high by even larger factors, since the production of C_4H_2 is strongly coupled to the C_2H_2 abundance. Our model abundances for C_2H_4 also fail to closely match the Voyager data. The model abundance is a factor of 3.5 high at 50°S, and it is low by the same factor at 50°N. Toublanc *et al.* (1995) had a more difficult time matching the Voyager C_2H_4 abundance; however, Lara *et al.* (1996) had quite good results.

In limiting the number of chemical reactions, the model did not incorporate the reaction

$$C_2H_3 + H + M \rightarrow C_2H_4 + M,$$

neglecting it in favor of the faster reaction

$$C_2H_3 + H \rightarrow C_2H_2 + H_2.$$

After this work was completed we became aware of calculations by Monke *et al.* (1995) showing that the above three-body reaction is much faster than previously thought. This reaction may now be important for the catalytic conversion of C_2H_2 into C_2H_6 in Titan's stratosphere. The absence of this reaction in the model may explain the high C_2H_2 and C_4H_2 mixing ratios.

As noted for all but one of the species in Table VI, both the Voyager data and the model show higher mixing ratios at 50°N than at 50°S. From our model we conclude that this may be an altitude effect in addition to a latitude effect. As the previously cited 1-D photochemical models have demonstrated, the mixing ratios for these hydrocarbon species increase with altitude. The contribution functions for the Voyager data for these species have maxima at higher altitudes for 50°N than for 50°S. We encourage the publication of the weighing function altitudes for the other latitudes so that we may determine to what extent the hydrocarbon enrichment at even higher northern latitudes is due to a real meridional enrichment and to what extent it is an altitude effect.

Some of the physical parameters incorporated into this work (e.g., K_{zz}, τ_r, and effect of aerosols on attenuating the solar flux) were taken from 1-D studies of Titan's atmosphere and relied on data that was either globally averaged or taken from limited latitude regions. One-dimensional models assume these parameters are a function of altitude only, but in reality these parameters are also functions of latitude and time (season). To keep the present

model simple, no attempt was made to determine meridional and seasonal variations in these parameters. Such an undertaking would be very difficult, if possible at all, with our limited knowledge of Titan's atmosphere.

Although this model limited the vertical extent of the atmospheric region of interest, the diffusive flux of molecular species through the upper boundary did incorporate meridional and season effects though the choice of the upper boundary conditions for the long-lived chemical species. These boundary conditions depend strongly on the temperature and photolysis rates at the upper boundary. The temperatures at the upper boundary are representative of the temperatures well above the boundary; however, the photodestruction rates of several of the chemical species (most importantly C_2H_6 and C_2H_4) are greater above the upper boundary than at the boundary. This likely introduces incorrect diffusive fluxes at the upper boundary and contributes to the shortcomings of the model.

This model was a first attempt at a simple 2-D photochemical transport model for Titan's stratosphere. Further modeling should be attempted which incorporates the coupling of photochemistry with radiative transfer and seasonal aerosol production models. Such coupling will result in more reliable seasonal temperature fields and photolysis rates. They should also be coupled with dynamical models that are accurate for a much greater vertical extent.

The Cassini mission is expected to monitor Titan between 2004 and 2008. This should add a wealth of new data on the seasonal variations in Titan's atmosphere as this mission will take place during early northern hemisphere winter, one season earlier than the Voyager encounters. Detailed meridional temperature data will allow for more accurate photochemical and dynamical modeling. In addition, close-up observations of atmospheric features should greatly improve our knowledge of zonal wind velocities which are needed in order to accurately determine meridional velocity fields for transport calculations.

ACKNOWLEDGMENTS

The author acknowledges D. F. Strobel for his enormous support in making this work possible. In addition, many thanks are owed to W. W. McMillan, Xun Zhu, F. M. Flasar, M. E. Summers.

REFERENCES

Akimoto, H., K. Obi, and I. Tanaka 1965. Primary processes in the photolysis of ethane at 1236 Å. *J. Chem. Phys.* **42**(11), 3864–3868.

Allen, M., J. P. Pinto, and Y. L. Yung 1980. Titan: Aerosol photochemistry and variations related to the sunspot cycle. *Astrophys. J.* **242**, L125–L128.

Andrews, D. G., J. R. Holton, and C. B. Leovy 1987. *Middle Atmosphere Dynamics.* Academic Press, Orlando.

Back, R. A. D., and W. L. Griffiths 1967. Flash photolysis of ethylene. *J. Chem. Phys.* **46**(12), 4839–4843.

Bézard, B., A. Coustenis, and C. P. McKay 1995. Titan's stratospheric temperature asymmetry: A radiative origin. *Icarus* **113**, 267–276.

Baulch, D. L., C. J. Cobos, R. A. Cox, C. Esser, P. Frank, T. Just, J. A. Ken, M. J. Pilling, J. Troe, R. W. Walker, and J. Warnatz 1992. Evaluated kinetic data for combustion modeling. *J. Phys. Chem. Ref. Data* **21**, 411–429.

Borrell, P., A. Cervenka, and J. W. Turner 1971. Pressure effects and quantum yields in the photolysis of ethylene and propene at 185 nm. *J. Chem. Soc. B* **1971**, 2293–298.

Broadfoot, A. L., A. L. Sandel, D. E. Shemansky, J. B. Holberg, G. R. Smith, D. F. Strobel, J. C. McConnell, S. Kumar, D. M. Hunten, S. K. Atreya, T. M. Donahue, H. W. Moos, J. L. Bertaux, J. E. Blamont, R. B. Pomphrey, and S. Linick 1981. Extreme ultraviolet observations from Voyager 1 encounter with Saturn. *Science* **212**, 206–211.

Caldwell, J. J. 1978. In *The Saturn System* (D. M. Hunten and D. M. Morrison, Eds.), NASA Conference Publication 2068, pp. 113–126.

Calvert, J. G., and J. N. Pitts 1966. *Photochemistry.* Wiley, New York.

Cogley, A. C., and W. J. Borucki 1976. Expeonential approximation for daily average solar heating or photolysis. *J. Atmos. Sci.* **33**, 1347–1356.

Collin, G. J. 1973. Photolyse du butene-1 dans l'ultraviolet a vide. Can. *J. Chem.* **51**, 2853–2859.

Collin, G. J., H. Deslauriers, and J. Deschenes 1979. Photolyse du propene et du methyl-2-butene-2 vers 174 et 163 nm. *Can. J. Chem.* **57**, 870–875.

Coustenis, A., and B. Bézard 1995. Titan's atmosphere from voyager infrared observations IV. Latitudinal variations of temperature and composition. *Icarus* **115**, 126–140.

Coustenis, A., B. Bézard, and D. Gautier 1989. Titan's atmosphere from Voyager infrared observations I. The gas composition of Titan's equatorial region. *Icarus* **80**, 54–76.

Coustenis, A., B. Bézard, D. Gautier, A. Marten, and R. Samuelson 1991. Titan's atmosphere from Voyager infrared observations III. Vertical distribution of hydrocarbons and nitriles near Titan's north pole. *Icarus* **89**, 152–167.

Flasar, F. M., and B. J. Conrath 1990. Titan's stratospheric temperatures: A case for dynamical inertia? *Icarus* **85**, 346–354.

Flasar, F. M., R. E. Samuelson, and B. J. Conrath 1981. Titan's atmosphere: Temperature and dynamics. *Nature* **292**, 693–698.

Gladstone, G. R., M. Allen, and Y. L. Yung 1996. Hydrocarbon photochemistry in the upper atmosphere of Jupiter. *Icarus* **119**, 1–52.

Hamai, S., and F. Hiryama 1979. Fluorescence of acetylenic hydrocarbons. *J. Chem. Phys.* **71**, 2934–2939.

Hampson, R. F., and J. R. McNesby 1965. Vacuum-ultraviolet photolysis of ethane at high temperature. *J. Chem. Phys.* **42**(6), 2200–2208.

Heck, A. J. R., R. N. Zare, and D. W. Chandler 1996. Photofragment imaging of methane. *J. Chem. Phys.* **104**(11), 4019–4030.

Heller, S. R., and G. W. A. Milne 1978. *EPA/NIH Mass Spectral Data Base* **1**, 30–186.

Hourdin, F., O. Talagrand, R. Sadourny, R. Courtin, D. Gautier, and C. P. McKay 1995. Numerical simulation of the general circulation of the atmosphere of Titan. *Icarus* **117**, 358–374.

Hutzell, W. T., C. P. McKay, O. B. Toon, and F. Hourdin 1996. Simulation of Titan's brightness by a two-dimensional haze model. *Icarus* **119**, 112–129.

Jacox, M. E., and D. E. Milligan 1974. Matrix isolation study of the vacuum ultraviolet photosys of allene and methylacetylene. Vibrational and electronic spectra of the species C_3, C_3H, CH_2, and C_3H_3. *Chem. Phys.* **4**, 45–61.

Kunde, V. G., A. C. Aikin, R. A. Hanel, D. E. Jennings, W. C. Maguire, and R. E. Samuelson 1981. C_4H_2, HC_3N, and C_2N_2 in Titan's atmosphere. *Nature* **292**, 686–688.

Lara, L. M., E. Lellouch, J. J. López-Moreno, and R. Rodrigo 1996. Vertical distribution of Titan's atmospheric neutral constituents. *J. Geophys. Res.* **101**, 23261–23283.

Lellouch, E., A. Coustenis, D. Gautier, F. Raulin, N. Dubouloz, and C. Frère 1989. Titan's atmosphere and hypothesized ocean: A reanalysis of the Voyager 1 radio-occultation and IRIS 7.7 mm data. *Icarus* **79**, 328–349.

Lias, S. G., G. J. Collin, R. E. Rebbert, and P. Ausloos 1970. Photolysis of ethane at 11.6–11.8 eV. *J. Chem. Phys.* **52**(4), 2934–2939.

Lindal, G., G. E. Wood, H. B. Hotz, D. N. Sweetnam, V. R. Eshleman, and G. L. Tyler 1983. The atmosphere of Titan: An analysis of the Voyager 1 radio occultation measurements. *Icarus* **53**, 348–363.

McMillan, W. W. 1992. *Revelations of a Stratospheric Circulation: The Dynamical Transport of Hydrocarbons in the Stratosphere of Uranus.* Ph.D. dissertation, The Johns Hopkins University.

Maguire, W. C., R. A. Hanel, D. E. Jennings, V. G. Kunde, and R. E. Samuelson 1981. C_3H_8 and C_3H_4 in Titan's atmosphere. *Nature* **292**, 683–686.

Monks, P. S., F. L. Nesbitt, W. A. Payne, M. Scanlon, L. J. Stief, and D. E. Shallcross 1995. Absolute rate constant and product branching ratios for the reaction between H and C_2H_3 at $T = 213$ and 298 K. *J. Phys. Chem.* **99**, 17151–17159.

Mount, G. H., and H. W. Moos 1978. Photoabsorbtion cross section of methane and ethane 1380–1600 Å, at $T = 295$ K and $T = 200$ K. *Astrophys. J.* **214**, L47–L49.

Nakayama, T., and K. Watanabe 1964. Absorption and photoionization coefficients of acetylene, propyne and 1-butyne. *J. Chem. Phys.* **40**(2), 558–561.

Okabe, H. 1981. Photochemistry of acetylene at 1470 Å. *J. Chem. Phys.* **75**, 2772–2778.

Okabe, H. 1983. Photochemistry of acetylene at 1849 Å. *J. Chem. Phys.* **78**, 1312–1317.

Prather, M. J. 1986. Numerical advection by conservation of second-order moments. *J. Geophys. Res.* **91**, 6671–6681.

Press, W. H., B. P. Flannery, S. A. Teukolsky, and W. T. Vetterling 1989. *Numerical Recipes: The Art of Scientific Computing.* Cambridge Univ. Press, Cambridge, UK.

Rabelais, J. W., J. M. McDonald, V. Scherr, and S. P. McGlynn 1971. Electronic microscopy of isoelectronic molecules. *Chem. Rev.* **71**(1), 94–95.

Samuelson, R. E., W. C. Maguire, R. A. Hanel, V. G. Kunde, D. E. Jennings, Y. L. Yung, and A. C. Aikin 1983. CO_2 on Titan. *J. Geophys. Res.* **88**, 8709–8715.

Shia, R. L., Y. L. Ha, J. S. Wen, and Y. L. Yung 1990. Two-dimensional atmospheric transport and chemistry model: Numerical experiments with a new advection algorithm. *J. Geophys. Res.* **95**, 7467–7483.

Smith, B. A., L. Solderblom, R. Beebe, J. Boyce, G. Briggs, A. Bunker, S. A. Collins, C. J. Hansen, T. V. Johnson, J. L. Mitchell, R. J. Terrile, M. Carr, A. F. Cook II, J. Cuzzi, J. B. Pollack, G. E. Danielson, A. Ingersoll, M. E. Davies, G. E. Hunt, H. Masursky, E. Shoemaker, D. Morrison, T. Owen, C. Sagan, J. Veverka, R. Strom, and V. E. Suomi 1981. Encounter with Saturn: Voyager 1 imaging science results. *Science* **212**, 163–191.

Sromovsky, L. A., V. E. Suomi, J. B. Pollack, R. J. Krauss, S. S. Limaye, T. Owen, H. E. Revercomb, and C. Sagan 1981. Implications of Titan's north–south brightness asymmetry. *Nature* **292**, 698–702.

Stief, L. J., V. J. De Carlo, and W. A. Payne 1971. Photochemistry of propyne at 1470 Å. *J. Chem. Phys.* **54**(A3), 1361–1368.

Strobel, D. F. 1974. The photochemistry of hydrocarbons in the atmosphere of Titan. *Icarus* **21**, 466–470.

Strobel, D. F., and D. E. Shemansky 1982. EUV emission from Titan's upper atmosphere: Voyager 1 encounter. *J. Geophys. Res.* **87**, 1361–1368.

Strobel, D. F., M. E. Summers, and X. Zhu 1993. Titan's upper atmospheric structure and ultraviolet emissions. *Icarus* **100**, 512–526.

Summers, M. E., and D. F. Strobel 1989. Photochemistry of the atmosphere of Uranus. *Astrophys. J.* **346** 495–508.

Sutcliffe, L. H., and A. D. Walsh 1952. The absorption spectrum of allene in the vacuum ultraviolet. *J. Chem. Soc.* **1952**, 899–905.

Toublanc, D., J. P. Parisot, J. Brillet, D. Gautier, F. Raulin, and C. P. McKay 1995. Photochemical modeling of Titan's atmosphere. *Icarus* **113**, 2–26.

Yelle, R. V. 1991. Non-LTE models of Titan's upper atmosphere. *Astrophys. J.* **383**, 380–400.

Yung, Y. L., M. Allen, and J. P. Pinto 1984. Photochemistry of the atmosphere of Titan: Comparison between model and observations. *Astrophys. Suppl. Ser.* **55**, 465–506.

Zelikoff, M., and K. Watanabe 1953. Absorption coefficients of ethylene in the vacuum ultraviolet. *J. Opt. Soc. Am.* **43**(9), 756–759.